Article

LA–ICP–MS U–Pb Dating, Elemental Mapping and In Situ Trace Element Analyses of Cassiterites from the Gejiu Tin Polymetallic Deposit, SW China: Constraints on the Timing of Mineralization and Precipitation Environment

Xiaohu He [1], Congfa Bao [2], Yongyan Lu [2], Nicole Leonard [3], Zheng Liu [1] and Shucheng Tan [1,*]

[1] School of Earth Scieces, Yunnan University, Kunming 650500, China; xhhe@ynu.edu.cn (X.H.); zhengliu@lzu.edu.cn (Z.L.)
[2] Yunnan Planning and Design Institute for Mineral and Land Resources, Kunming 650216, China; baocf2022@163.com (C.B.); lu1103210@163.com (Y.L.)
[3] School of Earth and Environmental Sciences, The University of Queensland, Brisbane, QLD 4072, Australia; n.leonard@uq.edu.au
* Correspondence: tansc001@126.com; Tel.: +86-0871-6503-3733

Abstract: As a major constituent in magmatic–hydrothermal ore deposits, cassiterites, with moderate amounts of U and low Pb, can be dated with U–Pb geochronology. The tetragonal lattice structure makes cassiterites capable of incorporating dozens of elements within its crystal lattice (e.g., Fe, Ti, W, Zr, Hf, Ta, Nb, Mn, Sc, V, and Sb). Variations of these elements record information of potential elemental substitution mechanisms and precipitation environments of cassiterites. In this study, we collected cassiterite grains from four different ore styles of the Gejiu tin polymetallic deposit to perform LA–ICP–MS U–Pb dating, multiple element mapping, and in situ trace element analysis on these cassiterites. Systematic U–Pb dating yielded Tera–Wasserburg lower intercepted ages at around 85 Ma, coinciding with zircon U–Pb ages of regional Late Yanshanian granitoids, within their respective analytical uncertainties. Such age coincidence, combined with the spatial association, suggests that tin mineralization may be genetically related to the Late Cretaceous granitic magmatism. Multielemental mapping shows that the distribution of Nb, Ta, and Ti in the cassiterite grains correlates well with the regular oscillatory zoning patterns in cathodoluminescence (CL) images. The relatively high Sb, Fe, W, Ga, and U concentrations control the dark luminescing domains in these cassiterite grains. The systematic variations in chemical compositions suggest that trace elements such as Sc, V, Fe, and Ga incorporate in cassiterites via coupled substitutions of $Sc^{3+} + V^{5+} \leftrightarrow 2 (Sn, Ti)^{4+}$, $Fe^{3+} + Ga^{5+} \leftrightarrow 2 (Sn, Ti)^{4+}$ and $Fe^{3+} + OH^- \leftrightarrow Sn^{4+} + O^{2-}$ or $Fe^{3+} + H^+ \leftrightarrow Sn^{4+}$. The covariation of redox sensitive elements such as W, U, Fe, and Sb indicates that the "tin-granite" type of cassiterites were formed under an oxidized state whereas cassiterites from skarn, massive sulfide, and oxidized ore styles were precipitated in a reducing environment.

Keywords: cassiterite; LA–ICP–MS mapping; U–Pb dating; trace element; precipitation environment; Gejiu

1. Introduction

Cassiterite (SnO_2) is the most important ore mineral for tin deposits and has a tetragonal lattice structure similar to that of the rutile group ($M^{4+}O_2$) [1–4]. Because cassiterite is resistant to chemical and physical alteration and weathering, trace elements, such as Fe, Ti, W, Zr, Hf, Ta, Nb, Mn, Sc, V, and Sb in cassiterite could be used to study mineralization processes and precipitation environments of tin mineralization [2–10]. Furthermore, the presence of U and Pb makes it possible to date cassiterite with U–Pb

geochronology [1,2,4,7–9,11–15]. Thus, cassiterite can be used to investigate mineralization timing, precipitation environment, and mechanisms for magmatic–hydrothermal ore deposits or important tin belts worldwide [3,4,16,17].

The world-class Gejiu tin polymetallic deposit in SW China has large metal reserves with an endowment estimated at ~10 million metric tonnes of tin, copper, lead, and zinc, containing approximately 300 Mt of tin and copper ore averaging 1 wt% Sn and 2 wt% Cu, respectively, and 400 Mt of lead–zinc ore with 7 wt% Pb + Zn [3,18,19]. Many attempts at dating mineralization timing have been conducted on hydrothermal minerals, including K–Ar/^{40}Ar–^{39}Ar dating on quartz/cassiterite [20], Pb–Pb dating on sulfide [20], Re–Os dating of molybdenite [21], and U–Pb dating of cassiterite [3,8,10,22]. However, there is still a lack of systematic cassiterite U–Pb dating of different ore styles. To trace the origins of ore-forming elements, many studies have focused on stable isotope compositions [23,24], but few studies have examined the composition of fluid inclusions to interpret the precipitation environments of the Gejiu deposit [10,22,24,25]. Thus, precipitation environments of cassiterite in hydrothermal fluids are poorly understood. Here, we study cassiterite grains from the Gejiu tin polymetallic deposit with U–Pb geochronology, elemental mapping, and in situ trace element geochemistry. Results allow us to discuss (1) the timing of Sn mineralization, (2) trace element concentration variations and elemental zoning in cassiterite, and (3) elemental substitution mechanisms and precipitation environments of cassiterites. These data could provide further insights into ore genesis in the world-class Gejiu tin district whilst highlighting the potential for using cassiterites as a monitor of hydrothermal processes and for understanding the timing and evolution of Sn mineralization events.

2. Regional Geological Setting and Deposit Geology

The Gejiu deposit in SW China is located along the boundary between the Tethys and Pacific tectonic domains and adjacent to the Ailao Shan–Red River (ASRR) shear zone (see Figure 1a). It is also adjacent to the Youjiang basin, which is bounded by the Mile–Shizong fault to the northwest, the Nandan–Duan fault to the northeast, the Pingxiang–Nanning fault to the southeast, and the NW-trending Honghe fault to the southwest (see Figure 1b, [26–28]). In the Gejiu mining district, almost all tin deposits are distributed to the east of the Gejiu fault, with numerous plutons but few deposits in the west. It can be divided into five east–west trending zones by major faults named Malage, Songshujiao, Gaosong, Laochang, and Kafang, from north to south into five ore fields. Extensive magmatic activity led to the development of numerous plutons consisting of gabbros, porphyritic and biotite granites, syenites, and metabasalts (see Figure 2, [29,30]).
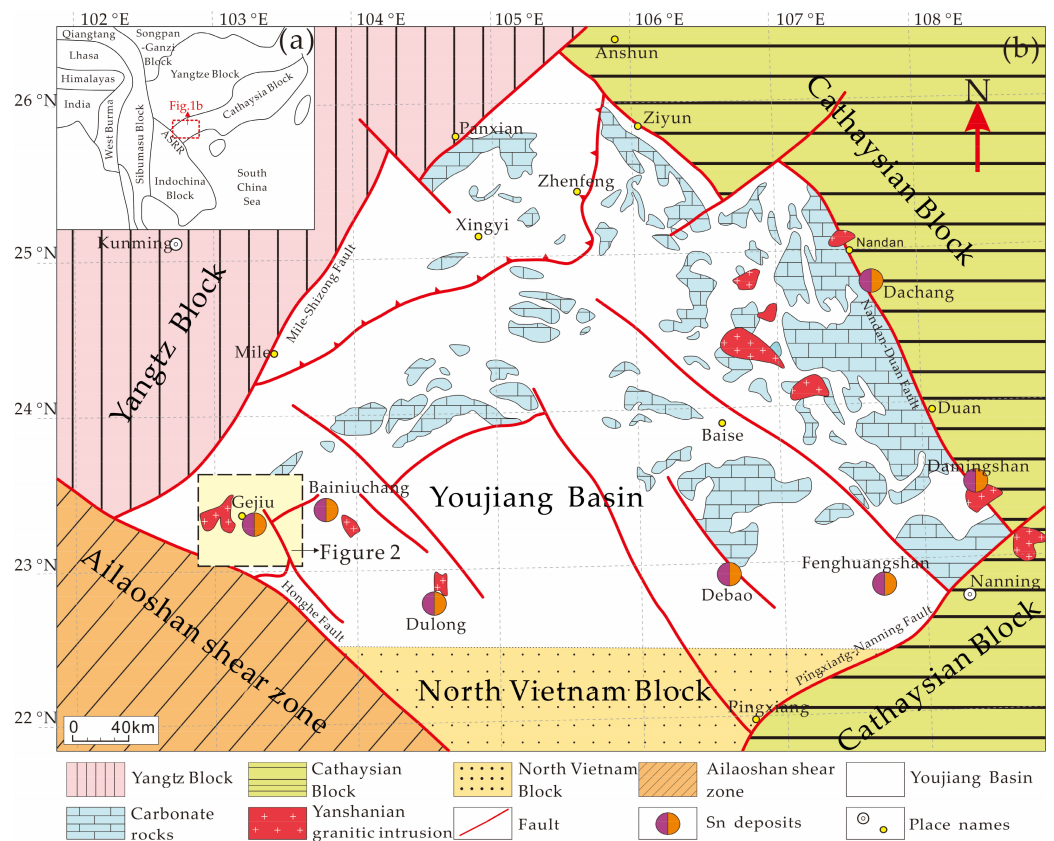
Figure 1. (**a**) Simplified geological map of eastern Asia, showing the major tectonic units [25,31], ASRR = Ailao Shan–Red River shear zone. (**b**) Geological map showing the distribution of tin deposits, including Gejiu in the Youjiang Basin, SW China (modified from [27,28]).

Previous studies suggest that granitoids in the Gejiu district were emplaced between 85 and 77 Ma [32,33], which is consistent with the Re–Os and ^{40}Ar–^{39}Ar ages (86 Ma ~ 77 Ma) of various ores from this deposit [10,30]. Excepting the absence of Late Triassic to Cretaceous strata due to episodic uplift, or erosion associated with Indosinian and Yanshanian tectonic events, Phanerozoic sedimentary stratum are well preserved in this district [8,18]. The strata largely consist of Middle Triassic Gejiu Formation carbonate sequences and the Falang Formation, which contains fine-grained clastic and carbonate sediments with intercalated mafic–felsic lavas (Figure 2b). Owing to extensive hydrothermal alteration, there are six ore styles, mainly composed of massive sulfide, oxidized ores, tin-granite, skarn, greisen, and veined tourmaline. Among them, skarn ores are the most widely distributed across the ore district and the most economically important [3]. Previous studies suggested that, except for the oxidized Sn ores, the other five types of Sn ores are considered to be related to the Yanshanian granitic magmatic activity [19,23,34]. However, several other studies suggested that the origin of the oxidized Sn ores is also closely related to the Gejiu granitic magmatic activity [25,29,30,33,35].
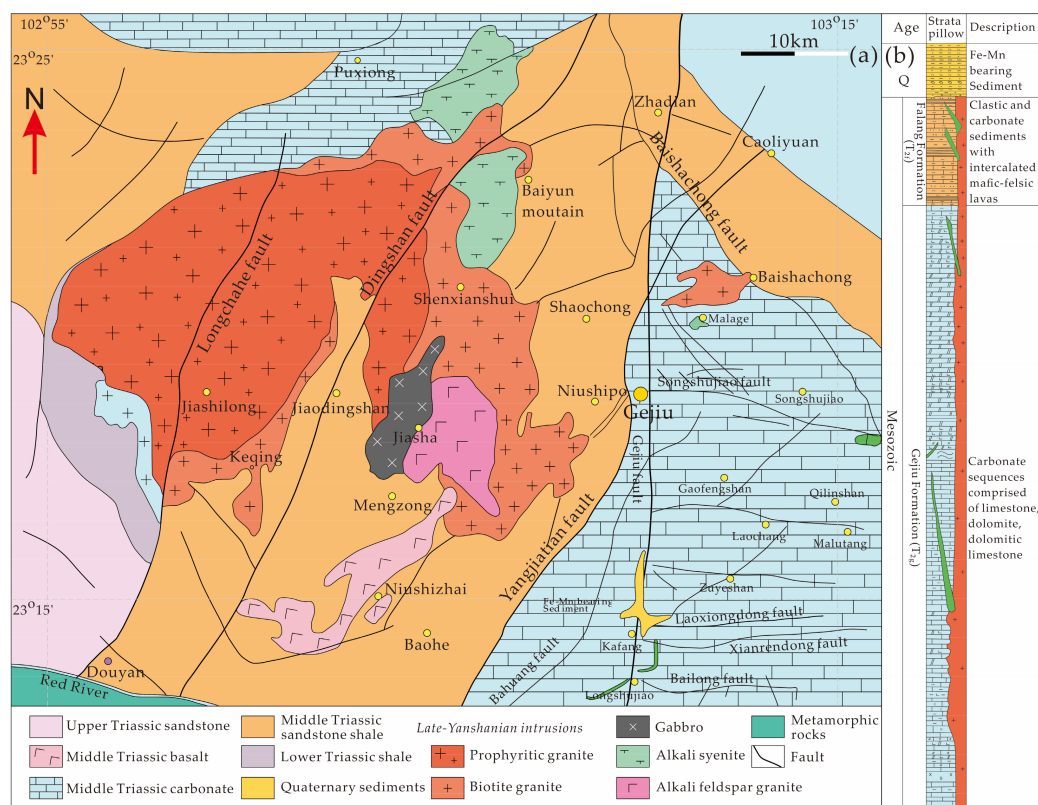
Figure 2. Regional geological map of the Gejiu ore district (**a**) and its strata (**b**) (modified from [3]).

3. Sample Description

We collected six cassiterite samples representing four different ore styles in the Gejiu Sn–polymetallic deposit. They include tin-granite (KF–03), skarn (KF–05), massive sulfide (LC–01, LC–02), and oxidized ores (SK–04, SK–05). Representative photographs of tin ores are shown in Figure 3. Cassiterite-bearing granite (hosting tin-granite) is not common in the ore district and considered as altered rock in a previous study [10]. Cassiterites hosted by tin-granite are dispersed in the granite, and their grains are always intergrown with fluorite and accompanied by tourmaline (Figure 3a). The skarn ores are mainly pyroxene- and garnet-rich with associated tremolite, actinolite, epidote, chlorite, fluorite, and tourmaline, with major ore minerals such as cassiterite, pyrrhotite, and chalcopyrite (Figure 3b). Massive sulfide ores comprise sulfides such as chalcopyrite, pyrrhotite, fluorite, azurite, scheelite, and cassiterite (Figure 3c). The oxidized ores are considered as loose earthy in this study; in previous studies, they may be named semioxidized stratiform or loose earthy ores in Triassic carbonate layers distal to granite [22,28]. Usually, they were thought to be products of the oxidation of primary sulfide ores and are dominated by hematite, limonite, pyrrhotite, and minor pyrite (Figure 3d). Most of them are hosted in Triassic carbonate layers and close to the surface and associated with small-scale faults [22].
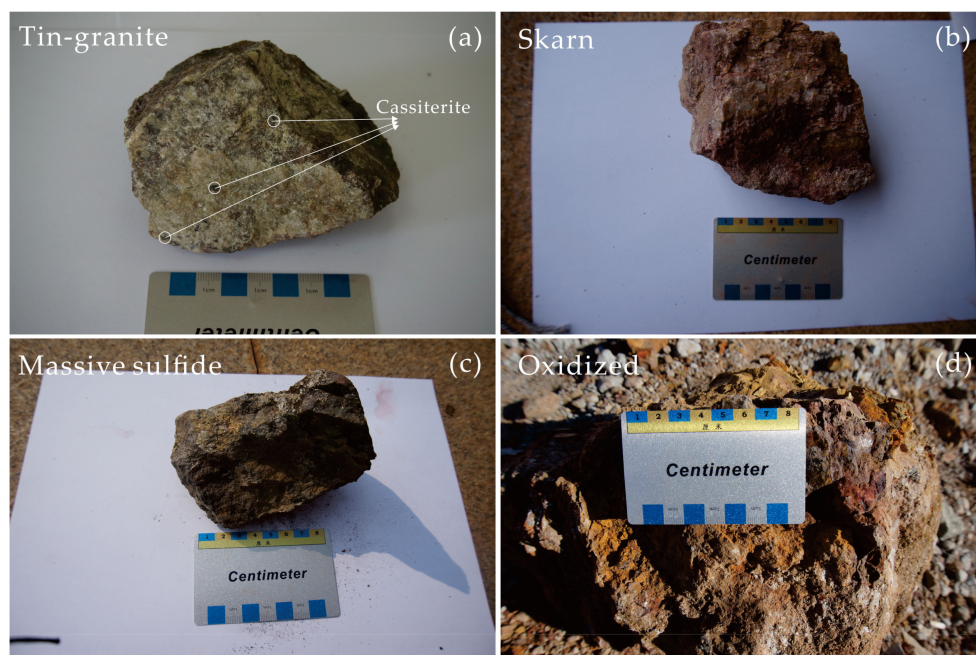
Figure 3. Representative photographs of tin ores from the Gejiu tin polymetallic deposit. (**a**) Tin-granite ore, also called cassiterite-bearing granite, which is only well developed in the interior of certain granite cupolas; (**b**) skarn ore is widely distributed in the contact zone of granite and carbonate, and contains garnet, pyroxene, epidote, and fluorite; (**c**) massive sulfide ore contains sulfide minerals; (**d**) red-brown oxidized ore is hosted in carbonate layers distal to intrusion and reveals a colloidal or honeycomb structure.

4. Analytical Methods

4.1. Cathodoluminescence Imaging

All samples were crushed and processed through conventional mineral separation processes. Cassiterite grains were handpicked under a binocular microscope and mounted in epoxy resin. To document internal structures and select potential targets for U–Pb analysis, cathodoluminescence (CL) images (Figure 4) were obtained using a scanning electron microscope. Backscattered electron (BSE) and cathodoluminescence (CL) images were taken using a Zeiss Supra 55 field emission scanning electron microscope (SEM, JSM–IT100, Japan Electron Optics Laboratory Co., Ltd., Tokyo, Japan) coupled with a cathodoluminescence detector at Wuhan Sample Solution Analytical Technology Co., Ltd. (Wuhan, China). Operating conditions included an accelerating potential of 10 kV, a temperature of 20 °C, and an image acquisition time of 35 s/sheet. To compare the CL images of cassiterite grains, specific analytical conditions were adopted during the experiment such that the instrument automatically adjusted the parameters to obtain an image with the highest resolution after the scale was changed.
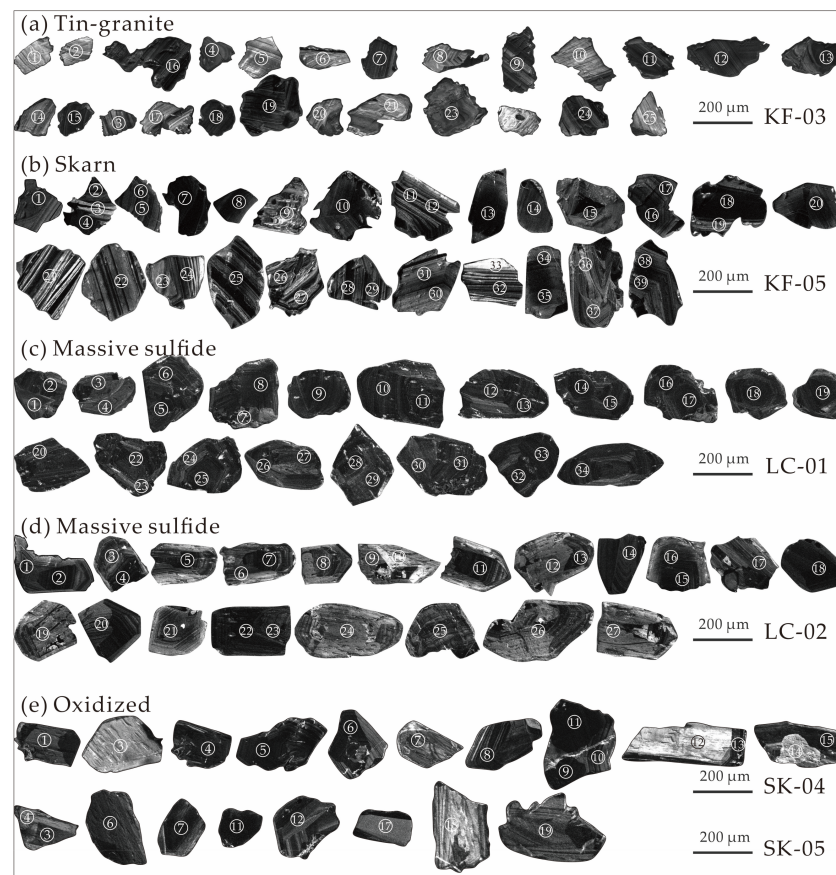
Figure 4. Representative cathodoluminescence images of the cassiterite samples from the Gejiu tin polymetallic deposit, showing internal textures of cassiterite grains. (**a**,**b**) Cassiterite grains from the tin–granite ore style display a regular oscillatory zoning; (**c**,**d**) Cassiterite grains from the massive sulfide ore style display an inner core with a regrowth rim; (**e**) Cassiterite grains from the oxidized ore style display an inner core and oscillatory zoning.

4.2. Cassiterite LA–ICP–MS U–Pb Dating

Cassiterite LA–ICP–MS U–Pb dating was performed at the Radiogenic Isotope Facility, The University of Queensland, Saint Lucia, QLD (Brisbane, Australia), using a Thermo iCAP RQ quadruple ICP–MS equipped with an ASI RESOlution SE 193 ArF nm excimer laser system. The laser was run with a 30 micron diameter round spot at 10 Hz, with a measured instrument laser-fluence (laser pulse energy per unit area) of 2.9 J/cm^2. For each spot, 10 s of blank was collected, followed by 20 s of ablation, and 5 s of washing. Helium gas carrying the ablated sample aerosol was mixed with argon (carrier gas) and nitrogen (additional diatomic gas) to enhance sensitivity to the ICP–MS instrument [1]. NIST–612 glass standard was employed for instrument tuning, achieving typical instrument sensitivity of about 40,000–50,000 cps/ppm ^{238}U with 100 μm laser spot size. A working standard (cassiterite AY–4, collected from the Anyuan tin deposit of the Furong district, South China, which has been well calibrated using ID–TIMS with a U–Pb age of 158.2 ± 0.4 Ma, 14) was used to correct the ^{206}Pb/^{238}U ratio. Operating conditions and analytical procedures were similar to those described by Nuriel et al. [36], Luo et al. [37], and Yang et al. [38]. Tera–Wasserburg concordia diagrams were processed using Isoplot 3.0 [39]. Data uncertainties of isotopic ratios are reported at 2σ level [1].

4.3. In Situ Trace Elemental Analysis and Mapping

In situ trace element analysis for cassiterite grains was performed at Wuhan Sample Solution Analytical Technology Co., Ltd., using an Agilent 7900 ICP–MS equipped with a GeolasHd 193 nm laser ablation system. Detailed operating conditions and the ICP–MS

instrument parameters are the same as those reported by Liu et al. [40]. Cassiterite grains were analyzed using a laser energy density of 3.46 J/cm^2, a spot size of 60 μm, and a laser pulse rate of 5 Hz. Multiple reference materials (NIST610, BCR–2G, BHVO–2G, and BIR–1G) were used as the bracketing external standard, ^{118}Sn was used as the internal standard, assuming stoichiometric SnO$_2$ for quantification purposes. The offline selection, integration of the background and analytical signals, time-drift correction, and quantitative calibration were processed using ICPMS DataCal 10.1 (China University of Geosciences, Wuhan, China) [41].

We used an ASI RESOlution 193 nm excimer UV ArF laser ablation system with a dual-volume Laurin Technic ablation cell, coupled to a Thermo iCap RQ quadruple mass spectrometer to perform elemental mapping at the Radiogenic Isotope Facility of The University of Queensland, Australia. The laser system was operated with GeoStar Norris software and the mass spectrometer with Qtegra software. Ablation was performed in ultrapure He (grade 5.0, 99.999% purity) to which the Ar make-up gas and a trace amount of N$_2$ was added for efficient transport and to aid ionization. The instrument was tuned with scans on NIST SRM 612 glass. Elemental maps were built with Iolite [42] v3.71 in quantitative mode, using NIST SRM 612 glass as calibration standard and Sn concentrations as internal standard. Accuracy and precision were monitored using BHVO–2G, BCR–2G, BIR–1G, and GSD–1G glass reference materials as quality monitor standards (http://georem.mpch--mainz.gwdg.de/, accessed on 29 November 2021). Accuracy was typically better than 1–10% and precision better than 1–5% (*n* = 5 for each glass reference material). Limits of detection were at the sub-ppm level for most analyzed elements and ≤2 ppm for Na and Cr. In this study, three types of cassiterite grains were investigated following the rastering technique described in Ubide et al. [43].

5. Results

5.1. Internal Structure Variations of Cassiterites

Cassiterite samples can be classified into two groups based on their CL images (Figure 4). The first group includes cassiterites from tin-granite and skarn ores, revealing dull luminescing and regular oscillatory zoning (see Figure 4a,b). The second group mainly includes cassiterites from massive sulfide and oxidized ores, revealing dark gray cores with dull rims and fine oscillatory zoning overgrowth (see Figure 4c–e). In general, cassiterite grains from tin-granite and skarn ores are largely free of inclusions with the exception of occasional micrometer-sized inclusions of scheelite and Fe-oxide. Notably, sulfide and oxidized cassiterites reveal an inner core with a regrowth rim, which is considered a dissolution–reprecipitation texture, indicating that the sulfide and oxidized cassiterite crystals may have undergone a dissolution–reprecipitation process. Whilst most cassiterite grains are dark (weak CL response), others appear highly luminescent in CL, and crystals often display regular variations between bright and dark CL. Internal zoning in cassiterite grains indicates that variations in CL signals may be due to intragrain scale compositional variations, which is proved by the elemental variation shown by elemental mappings in the following text.

5.2. Cassiterite LA–ICP–MS U–Pb Ages

Based on reverberation and transmission photos and CL images, we chose domains without mineral or fluid inclusions and cracks to perform U–Pb isotope analyses for dating the cassiterite. The LA–ICP–MS U–Pb dating results are provided in Table 1 and Figure 5. Isotopic ratios show large variations with ^{238}U/^{206}Pb in the range of 3.937–87.642 and ^{207}Pb/^{206}Pb in the range of 0.047–0.849. Samples yielded Tera–Wasserburg concordia lower-intercept ages at around 85 Ma. The plots of tin-granite sample (KF–03, Figure 5a) yielded a Tera–Wasserburg concordia lower-intercept age of 85.5 ± 1.0 Ma (2σ, *n* = 29, MSWD = 2.7), the plots of skarn sample (KF–05, Figure 5b) yielded a Tera–Wasserburg concordia lower-intercept age of 85.90 ± 0.41 Ma (2σ, *n* = 39, MSWD = 0.92), the plots of tin-granite sample (LC–01, Figure 5c) yielded a Tera–Wasserburg concordia lower-intercept age of 85.2 ± 1.0 Ma (2σ, *n* = 43, MSWD = 3.7), respectively. The age results are consistent with

the zircon U–Pb ages of Late Yanshanian granitoids (77.4–85.0 Ma, according to Cheng and Mao [33]) in this district within a reasonable error range. These concordia ages represent the mineralization timing of the Gejiu tin polymetallic deposits.

Table 1. U–Pb isotopic ratios of cassiterite samples analyzed by LA–ICP–MS single spot analysis.

Spot No.	U (ppm)	2S	$^{238}U/^{206}Pb$	2S	$^{207}Pb/^{206}Pb$	2S
KF-03-01	1.46	0.04	3.937	0.527	0.849	0.023
KF-03-02	7.55	0.14	25.253	4.655	0.442	0.043
KF-03-03	52.6	0.41	82.988	1.928	0.058	0.004
KF-03-04	42.6	0.51	83.612	1.818	0.050	0.003
KF-03-05	70.4	0.70	84.175	1.630	0.055	0.003
KF-03-06	1.02	0.03	69.444	8.198	0.262	0.075
KF-03-07	67.7	0.77	60.864	1.148	0.283	0.007
KF-03-08	54.4	0.73	85.106	1.811	0.048	0.003
KF-03-09	44.8	0.40	82.034	1.884	0.048	0.003
KF-03-10	10.8	0.41	77.761	3.144	0.087	0.011
KF-03-11	40.7	0.31	83.612	2.027	0.047	0.003
KF-03-12	20.3	0.56	62.305	2.446	0.267	0.020
KF-03-13	9.69	0.21	18.553	3.098	0.531	0.043
KF-03-14	24.6	0.41	60.241	3.992	0.241	0.032
KF-03-15	2.91	0.0	67.751	4.269	0.163	0.025
KF-03-16	5.78	0.11	32.573	1.592	0.564	0.027
KF-03-17	10.9	0.45	82.508	2.995	0.068	0.006
KF-03-18	50.3	0.58	58.824	3.806	0.254	0.024
KF-03-19	3.50	0.22	77.160	4.823	0.143	0.023
KF-03-20	26.8	0.81	68.306	1.820	0.188	0.011
KF-03-21	18.7	0.77	31.546	5.175	0.433	0.036
KF-03-22	1.96	0.048	40.984	4.367	0.559	0.062
KF-03-23	0.56	0.039	18.182	6.612	0.430	0.100
KF-03-24	20.3	0.26	54.855	1.414	0.367	0.013
KF-03-25	1.61	0.07	69.444	6.269	0.214	0.041
KF-03-26	42.3	0.50	75.643	2.060	0.112	0.010
KF-03-27	40.0	0.40	75.131	4.911	0.106	0.021
KF-03-28	2.82	0.51	63.291	6.409	0.286	0.061
KF-03-29	44.5	1.60	83.963	1.762	0.051	0.003
KF-05-01	25.4	0.66	6.075	0.351	0.781	0.011
KF-05-02	4.15	0.14	56.497	4.150	0.289	0.036
KF-05-03	15.6	0.13	73.746	1.849	0.128	0.010
KF-05-04	3.02	0.18	79.051	4.249	0.074	0.014
KF-05-05	21.6	0.31	80.451	1.812	0.073	0.004
KF-05-06	9.57	0.15	72.254	3.289	0.136	0.016
KF-05-07	13.0	0.43	83.403	2.365	0.060	0.005
KF-05-08	12.8	0.22	82.372	2.036	0.060	0.004
KF-05-09	19.4	0.20	64.516	1.915	0.220	0.013
KF-05-10	2.57	0.06	79.365	2.331	0.074	0.007
KF-05-11	11.4	0.19	79.745	2.480	0.071	0.007
KF-05-12	3.99	0.13	79.808	1.847	0.066	0.005
KF-05-13	11.6	0.11	82.034	1.952	0.061	0.004
KF-05-14	3.50	0.15	76.278	4.596	0.117	0.021
KF-05-15	15.9	0.26	82.034	2.355	0.068	0.007
KF-05-16	13.7	0.11	80.128	1.926	0.061	0.005
KF-05-17	24.5	0.40	57.438	1.551	0.297	0.013
KF-05-18	22.6	0.67	76.511	2.400	0.111	0.008
KF-05-19	25.9	2.00	81.037	1.773	0.069	0.004
KF-05-20	14.5	0.43	53.533	2.149	0.330	0.019
KF-05-21	43.3	0.98	77.160	3.929	0.072	0.013
KF-05-22	17.6	0.43	63.654	2.634	0.243	0.020
KF-05-23	38.4	2.00	82.919	1.925	0.057	0.004
KF-05-24	33.6	0.64	82.988	2.273	0.051	0.004

Table 1. *Cont.*

Spot No.	U (ppm)	2S	^{238}U/^{206}Pb	2S	^{207}Pb/^{206}Pb	2S
KF-05-25	8.82	0.16	80.841	2.222	0.051	0.005
KF-05-26	15.6	0.25	82.102	1.955	0.053	0.003
KF-05-27	25.8	0.43	23.256	0.919	0.601	0.025
KF-05-28	11.4	0.16	83.542	2.024	0.048	0.004
KF-05-29	29.9	0.63	83.056	1.587	0.055	0.002
KF-05-30	87.9	1.50	81.633	1.933	0.057	0.003
KF-05-31	22.7	0.38	78.989	2.246	0.078	0.007
KF-05-32	29.1	0.32	81.967	2.687	0.050	0.005
KF-05-33	18.7	0.17	83.056	2.414	0.050	0.004
KF-05-34	11.2	0.15	80.841	1.634	0.088	0.005
KF-05-35	80.9	1.10	82.305	1.490	0.056	0.002
KF-05-36	16.8	0.31	81.833	3.080	0.059	0.007
KF-05-37	20.2	1.00	80.906	2.291	0.051	0.005
KF-05-38	18.1	0.26	82.988	2.617	0.058	0.006
KF-05-39	4.59	0.27	85.911	3.764	0.060	0.009
LC-01-01	15.8	0.51	66.756	2.897	0.180	0.021
LC-01-02	13.1	0.43	70.771	2.504	0.175	0.014
LC-01-03	14.4	0.22	77.640	2.230	0.060	0.005
LC-01-04	20.3	0.24	59.312	1.618	0.294	0.012
LC-01-05	14.7	0.99	65.963	2.132	0.214	0.019
LC-01-06	34.4	0.52	87.642	1.997	0.069	0.004
LC-01-07	10.6	0.49	68.027	2.962	0.194	0.021
LC-01-08	10.6	0.46	34.602	1.437	0.523	0.021
LC-01-09	6.83	0.09	71.994	2.954	0.119	0.012
LC-01-10	13.8	0.39	74.963	2.248	0.119	0.010
LC-01-11	17.9	0.20	72.202	2.085	0.309	0.019
LC-01-12	2.33	0.05	82.440	5.505	0.071	0.019
LC-01-13	5.35	0.15	79.177	3.824	0.059	0.011
LC-01-14	140	3.90	83.893	1.478	0.049	0.002
LC-01-15	16.4	0.28	39.526	2.031	0.454	0.020
LC-01-16	18.3	0.51	74.239	2.645	0.108	0.010
LC-01-17	12.7	0.17	83.612	2.657	0.075	0.007
LC-01-18	10.9	0.17	84.746	2.873	0.058	0.007
LC-01-19	30.5	0.39	80.645	1.886	0.097	0.006
LC-01-20	18.1	0.59	83.264	2.288	0.057	0.004
LC-01-21	14.2	0.18	81.633	2.399	0.065	0.006
LC-01-22	6.77	0.48	42.373	16.88	0.127	0.031
LC-01-23	10.4	0.12	77.042	2.552	0.102	0.011
LC-01-24	12.2	0.54	41.152	1.863	0.433	0.022
LC-01-25	22.8	0.24	66.050	1.614	0.239	0.012
LC-01-26	14.6	0.34	68.353	2.803	0.183	0.021
LC-01-27	8.72	0.58	77.700	3.381	0.090	0.011
LC-01-28	10.2	0.73	78.555	2.962	0.087	0.009
LC-01-29	28.6	0.43	80.386	2.068	0.064	0.006
LC-01-30	18.7	0.22	71.633	2.720	0.146	0.019
LC-01-31	6.53	0.10	79.554	3.164	0.060	0.008
LC-01-32	4.78	0.06	76.453	3.682	0.141	0.017
LC-01-33	31.7	0.43	82.919	1.856	0.059	0.004
LC-01-34	8.89	0.12	83.682	3.011	0.050	0.005
LC-01-35	17.7	0.37	76.453	2.163	0.158	0.011
LC-01-36	8.86	0.51	69.735	2.431	0.204	0.017
LC-01-37	17.1	0.33	79.365	2.079	0.081	0.006
LC-01-38	35.0	0.60	82.508	1.838	0.057	0.003
LC-01-39	22.1	0.20	75.245	2.038	0.114	0.009
LC-01-40	6.95	0.11	62.189	2.746	0.258	0.021
LC-01-41	31.8	0.34	79.681	1.841	0.084	0.005
LC-01-42	28.4	0.24	64.851	1.346	0.234	0.008
LC-01-43	22.5	0.73	61.996	2.537	0.226	0.026
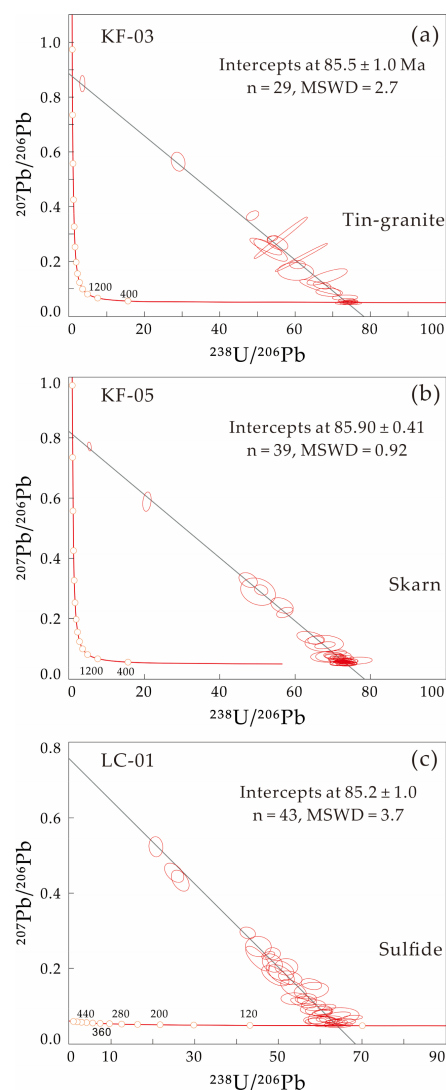
Figure 5. Tera–Wasserburg U–Pb plots for cassiterites from the Gejiu tin polymetallic deposit (the ages are calculated at 95% confidence level). (**a**) Plots reveal a mineralization age at 85.5 ± 1.0 Ma; (**b**) Plots reveal a mineralization age at 85.90 ± 0.41 Ma; (**c**) Plots reveal a mineralization age at 85.2 ± 1.0 Ma.

5.3. Trace Element Composition and Mapping

Cassiterite grains from different types of cassiterite-bearing ores were analyzed for trace elements, and at least 20 analyses were performed on every cassiterite sample. The analysis results of in situ trace elements for cassiterites are listed in Table 2. The most abundant trace elements in the analyzed cassiterites were Fe (40.73 to >8400 ppm), W (0 to >8500 ppm), Ti (14 to >8400 ppm), and Sc (0–727 ppm). Nb (0–1616 ppm), Ta (0–523 ppm), V (0–822 ppm), Zr (0–483 ppm), Sb (0–229 ppm), and U (0–67.8 ppm) concentrations were also relatively high and vary over several orders of magnitude, even within a single sample of an ore type. Co (8.91–11.96 ppm), Ni (63.1–89.46 ppm) concentrations are relatively constant and Ni/Co ratios (6.59–8.10) vary slightly. Other elements such as Cd, Cu, Zn, Ag, Mo, Rb, Sr, Th, Pb, and REEs were consistently determined to be close to or below detection limits. Hf concentrations were generally below 20 ppm (average value = 4.17 ppm), with U concentrations below 68 ppm.

Table 2. Trace element composition of tin-granite, skarn, and massive sulfide types of cassiterite samples analyzed by LA–ICP–MS single spot analysis.

	SnO$_2$	FeO^T	TiO$_2$	SiO$_2$	Al$_2$O$_3$	Sc	V	Cr	Co	Ni	Ga	Zr	Nb	Sb	Hf	Ta	W	U
Spot No.			wt%									ppm						
Tin-granite type																		
KF-03-01	99.1	0.120	0.460	0.150	0.0019	423	105	3.10	10.4	75.9	2.71	133	212	2.27	8.35	33.9	4.62	1.73
KF-03-02	99.0	0.210	0.440	0.120	0.0021	417	95.7	3.00	10.8	78.1	2.95	144	944	2.87	9.90	45.1	3.57	2.76
KF-03-03	98.2	0.038	1.36	0.130	0.0005	63.9	2.60	2.60	10.2	81.2	0.380	72.2	349	30.0	4.77	40.8	1294	10.0
KF-03-04	98.7	0.045	0.680	0.130	0.0007	92.4	14.2	3.09	10.1	77.3	0.700	176	787	13.1	9.50	101	1919	41.5
KF-03-05	98.5	0.150	1.04	0.150	0.0029	313	59.9	12.20	9.58	75.5	4.08	73.6	446	5.02	4.19	36.3	3.37	3.62
KF-03-06	98.8	0.120	0.770	0.150	0.0051	163	34.1	2.07	10.3	79.9	3.84	159	577	2.39	9.51	67.6	28.1	4.32
KF-03-07	98.6	0.042	0.830	0.150	0.0009	137	16.5	2.50	9.82	79.6	0.72	163	719	13.6	8.27	105	1695	35.4
KF-03-08	99.1	0.081	0.490	0.160	0.0034	254	39.7	4.97	10.1	77.5	3.20	138	548	1.31	8.91	64.5	13.9	2.66
KF-03-09	98.9	0.036	0.640	0.150	0.0006	48.5	7.36	0.06	10.3	71.8	0.750	185	299	37.9	10.5	32.4	1208	49.9
KF-03-10	99.2	0.091	0.350	0.140	0.0009	276	64.5	6.96	9.74	78.7	1.49	108	624	1.49	8.94	80.9	2.61	0.880
KF-03-11	98.7	0.044	0.750	0.130	0.0007	98.4	14.6	3.13	10.1	74.3	0.750	174	829	14.7	9.52	130	1599	37.3
KF-03-12	98.6	0.042	0.830	0.140	0.0007	155	18.1	1.43	9.72	73.8	0.860	156	731	13.8	7.32	75.1	1908	34.2
KF-03-13	98.0	0.052	1.51	0.130	0.0006	46.4	4.53	1.31	10.1	71.4	0.610	68.1	996	15.3	4.16	154	805	6.58
KF-03-14	99.1	0.130	0.470	0.140	0.0014	257	71.7	5.60	9.95	72.9	2.28	118	366	2.21	8.51	50.8	1.39	1.44
KF-03-15	98.0	0.093	1.23	0.150	0.0008	65.1	15.6	4.73	9.83	70.6	1.25	138	1112	30.1	7.25	119	2378	38.3
KF-03-16	98.2	0.074	1.23	0.150	0.0007	47.7	8.70	1.47	10.1	74.7	1.45	148	889	40.6	7.55	62.2	1366	38.8
KF-03-17	99.3	0.078	0.320	0.130	0.0009	186	49.2	6.25	10.0	71.5	1.42	101	431	1.47	8.46	71.7	1.33	0.700
KF-03-18	98.7	0.048	0.650	0.110	0.0007	67.1	10.3	—	9.93	78.8	0.530	171	314	15.0	9.40	78.0	2563	46.3
KF-03-19	98.8	0.130	0.720	0.120	0.0013	121	164	12.70	9.91	73.2	2.85	104	913	3.23	8.40	15.5	5.57	1.23
KF-03-20	99.1	0.098	0.520	0.130	0.0028	314	93.0	7.58	10.1	75.7	3.29	142	169	1.89	8.74	21.3	2.00	1.58
KF-03-21	99.2	0.100	0.460	0.130	0.0051	208	40.3	5.14	10.2	75.4	5.07	97.5	257	1.96	6.34	52.6	19.0	2.70
KF-03-22	97.4	0.062	1.98	0.140	0.0009	26.7	4.51	4.14	9.74	73.5	0.89	73.5	538	12.7	3.97	88.7	2503	12.1
KF-03-23	99.0	0.059	0.690	0.120	0.0009	119	37.9	14.0	9.97	72.7	1.31	68.5	332	2.13	6.13	35.6	0.87	0.290
KF-03-24	98.1	0.082	1.23	0.130	0.0006	60.8	13.2	5.97	9.63	74.0	1.10	153	1192	41.0	8.22	110	1579	42.6
KF-03-25	99.2	0.078	0.320	0.130	0.0006	158	95.6	10.30	10.1	75.6	0.910	84.5	832	1.80	11.7	236	2.83	0.530
Skarn type																		
KF-05-01	98.8	0.830	0.150	0.114	0.019	44.0	6.88	—	10.3	78.5	26.4	36.0	206	43	3.76	15.1	119	18.7
KF-05-02	99.0	0.550	0.160	0.113	0.0093	239	21.6	1.74	10.0	76.4	17.6	18.5	340	46	2.01	21.7	84.9	6.08
KF-05-03	99.5	0.130	0.110	0.105	0.0041	50.9	10.04	0.34	10.3	80.7	5.29	37.9	300	4.7	4.97	133	97.0	2.06
KF-05-04	99.4	0.035	0.026	0.122	0.0018	0.230	0.024	—	11.3	83.8	2.17	23.2	89.1	22	1.84	6.75	2823	38.0
KF-05-05	98.8	0.820	0.093	0.16	0.0200	37.0	7.15	0.01	11.0	89.2	26.4	48.4	31.6	18.5	5.06	3.66	29.1	8.37
KF-05-06	98.9	0.790	0.092	0.140	0.0200	37.5	7.39	—	12.0	89.5	25.7	44.9	27.3	17.2	5.73	1.68	44.7	8.27
KF-05-07	99.1	0.170	0.036	0.123	0.0130	10.4	1.39	0.05	11.7	82.5	6.58	25.6	547	11.8	2.93	78.1	3873	15.7
KF-05-08	99.0	0.770	0.030	0.119	0.0190	21.8	4.13	—	11.1	81.6	25.0	1.76	12.3	17.5	0.35	2.97	19.0	7.93
KF-05-09	99.2	0.160	0.330	0.125	0.0029	120	14.2	1.76	11.0	81.4	4.60	96.0	378	3.3	12.6	148	4.36	0.960
KF-05-10	98.2	0.580	0.710	0.140	0.0126	281	122	6.15	10.6	81.8	15.5	116	1175	13.3	11.4	83.1	48.2	10.6
KF-05-11	98.9	0.690	0.130	0.132	0.0140	175	28.9	1.10	10.8	78.8	25.5	12.3	86.5	31	1.42	50.8	22.6	5.92
KF-05-12	99.1	0.170	0.033	0.118	0.0124	3.14	1.25	0.360	11.0	77.9	8.73	14.4	180	11.8	1.70	53.5	3958	19.2
KF-05-13	98.9	0.800	0.049	0.107	0.0180	15.2	2.20	0.360	10.8	79.7	23.9	10.6	53.8	51	0.76	0.440	122	25.3
KF-05-14	98.7	0.630	0.300	0.140	0.0130	96.4	25.0	1.17	10.4	78.8	18.0	66.9	715	24	7.15	114	87.4	14.5
KF-05-15	98.4	0.320	0.450	0.130	0.0076	727	371	6.82	11.0	83.2	7.38	171	1616	10.7	19.3	55.7	1592	14.5
KF-05-16	99.3	0.360	0.103	0.119	0.0096	155	34.5	1.10	10.7	75.5	10.9	103	83.9	13.5	13.3	2.30	13.6	5.95
KF-05-17	99.0	0.640	0.150	0.122	0.0140	44.3	9.78	—	11.6	80.4	20.2	41.9	149	20	5.32	4.42	62.9	8.85
KF-05-18	99.0	0.830	0.014	0.102	0.0190	10.1	0.72	0.920	10.5	81.7	32.0	1.47	18.0	38	0.14	2.74	61.0	13.9
KF-05-19	99.4	0.160	0.170	0.116	0.0046	28.1	6.66	1.98	10.5	83.6	6.19	25.0	266	2.7	3.76	252	6.85	1.57
KF-05-20	98.0	0.490	0.960	0.132	0.0115	370	132	21.2	11.0	78.4	13.0	119	1474	12.5	12.6	327	39.3	7.32
KF-05-21	99.6	0.160	0.027	0.140	0.0048	3.12	0.840	0.420	11.1	82.8	6.38	37.3	44.2	3.0	4.64	12.7	8.88	1.76
KF-05-22	98.9	0.520	0.290	0.117	0.0109	167	16.3	1.36	11.1	81.0	14.8	32.5	385	12.8	3.39	20.5	10.3	5.50
KF-05-23	99.5	0.170	0.062	0.120	0.0040	682	51.5	—	11.5	78.4	4.75	53.2	115	11.6	5.89	19.8	6.58	1.15
KF-05-24	99.0	0.390	0.260	0.120	0.0050	191	33.1	1.71	10.8	77.7	11.1	28.0	626	36	4.34	155	88.7	5.47
KF-05-25	99.0	0.500	0.140	0.118	0.0131	602	27.8	0.290	11.0	76.4	16.8	25.1	236	23	2.95	77.0	75.7	3.15
KF-05-26	99.3	0.330	0.160	0.099	0.0060	178	21.4	—	10.7	79.9	10.9	26.4	225	21	3.12	92.7	39.4	3.08
KF-05-27	99.5	0.300	0.021	0.120	0.0126	4.95	2.47	0.270	10.9	77.6	15.8	10.2	43.7	7.4	1.03	10.5	28.7	3.34
KF-05-28	99.0	0.770	0.042	0.125	0.0190	42.4	3.12	0.160	11.1	78.5	30.6	13.5	40.0	34	1.61	15.0	42.9	5.95
KF-05-29	98.9	0.690	0.170	0.119	0.0120	447	26.8	0.700	10.5	82.2	22.2	14.5	204	33	1.99	3.73	24.5	5.35
KF-05-30	98.7	0.750	0.340	0.115	0.0170	63.7	17.9	2.52	10.3	80.7	23.0	55.3	212	16.6	5.73	62.9	27.8	9.70
KF-05-31	98.6	0.700	0.430	0.129	0.0140	31.4	10.97	1.53	10.7	80.7	20.8	62.3	232	14.4	6.95	87.3	25.9	10.7
KF-05-32	99.0	0.560	0.140	0.126	0.0084	233	16.7	0.390	11.1	79.4	16.3	20.2	413	54	2.77	32.8	82.3	7.22
KF-05-33	99.6	0.036	0.170	0.119	0.0009	72.2	9.79	0.820	10.7	77.5	1.12	22.9	135	2.1	4.18	197	12.0	0.13
KF-05-34	98.8	0.640	0.340	0.115	0.0137	133	43.7	1.14	11.2	77.5	17.8	18.6	295	12.8	1.87	19.6	15.5	8.58
KF-05-35	98.9	0.830	0.095	0.118	0.0210	58.4	37.3	0.930	11.1	78.8	25.0	7.64	51.1	21	0.89	8.77	26.7	10.1
KF-05-36	99.4	0.200	0.160	0.132	0.0046	158	13.8	2.07	11.1	76.9	6.36	61.9	352	6.7	7.35	174	10.2	2.59
KF-05-37	99.3	0.340	0.105	0.120	0.0080	114	8.53	1.26	11.0	79.9	13.6	28.6	443	21	3.66	81.7	19.1	5.16
KF-05-38	98.8	0.840	0.096	0.118	0.0200	61.7	12.3	—	10.7	77.3	26.2	24.9	46.0	23	2.75	1.65	33.2	11.6
KF-05-39	98.9	0.870	0.056	0.110	0.0220	37.0	12.6	1.86	10.9	79.9	28.2	30.4	17.3	20	3.69	1.20	25.8	9.06
Massive sulfide type																		
LC-01-01	98.9	0.160	0.011	0.820	0.0044	22.0	42.3	—	10.5	75.6	1.61	60.4	12.0	9.10	3.01	3.47	2.81	0.940
LC-01-02	93.0	0.730	0.020	4.11	1.3200	56.3	58.6	0.970	9.71	71.6	8.94	50.4	461	90.9	2.34	57.6	2345	17.9
LC-01-03	99.8	0.460	0.021	0.810	0.0190	72.4	79.8	0.530	10.4	75.5	5.42	35.7	36.4	36.4	1.59	54.5	14.2	5.35
LC-01-04	99.0	0.140	0.012	0.710	0.0081	19.3	22.4	0.480	10.3	73.6	1.12	68.0	427	18.3	3.80	62.9	92.2	3.29
LC-01-05	86.1	1.210	0.026	8.57	2.9000	79.5	109	1.50	8.98	68.8	12.7	80.1	914	55.6	4.74	146	900	11.9
LC-01-06	98.9	0.150	0.009	0.79	0.0047	28.4	77.9	0.600	10.6	79.7	1.58	69.1	231	17.4	3.28	28.4	524	5.00
LC-01-07	98.1	0.660	0.039	0.760	0.0210	131	69.9	2.27	10.2	77.8	5.97	141	1400	79.0	9.29	523	106	14.6
LC-01-08	98.6	0.450	0.017	0.780	0.0160	132	222	1.17	10.5	76.7	5.44	105	113	39.2	6.30	44.0	15.2	6.36
LC-01-09	98.7	0.170	0.016	0.730	0.0120	17.9	18.6	0.390	10.3	74.6	1.63	24.8	132	69.8	0.99	10.9	2514	11.0
LC-01-10	98.7	0.150	0.008	0.860	0.0070	16.8	17.2	0.800	11.2	79.8	1.61	37.4	183	51.3	1.68	38.1	1647	10.2
LC-01-11	98.5	0.260	0.025	0.840	0.0100	67.8	121	2.25	10.1	76.0	2.97	77.0	1379	23.3	5.50	224	555	8.86
LC-01-12	98.3	0.710	0.024	0.740	0.0220	86.9	72.3	1.64	10.4	75.6	8.73	61.4	395	121	3.21	26.9	72.9	14.4
LC-01-13	98.8	0.140	0.021	0.750	0.0069	14.8	16.1	—	10.7	76.8	1.41	37.4	135	48.3	1.85	32.7	1842	9.26
LC-01-14	98.3	0.480	0.021	0.840	0.0380	63.1	54.2	—	10.5	76.5	6.59	50.8	258	90.5	2.27	12.6	1500	16.8
LC-01-15	98.5	0.160	0.016	0.940	0.0064	28.9	52.4	—	10.5	76.0	1.84	55.1	206	54.9	2.28	11.2	2359	11.6
LC-01-16	99.3	0.170	0.050	0.092	0.0072	31.5	62.8	—	10.6	76.6	1.44	58.7	593	72.7	2.93	62.8	2143	13.3
LC-01-17	98.5	0.500	0.023	0.740	0.0210	161	231	—	9.97	76.7	6.99	96.1	483	73.9	5.21	93.1	310	9.83

Table 2. *Cont.*

Spot No.	SnO$_2$	FeO^T	TiO$_2$	SiO$_2$	Al$_2$O$_3$	Sc	V	Cr	Co	Ni	Ga	Zr	Nb	Sb	Hf	Ta	W	U
			wt%									ppm						
Massive sulfide type																		
LC-01-18	98.7	0.330	0.020	0.750	0.0120	154	337	3.86	10.5	77.0	4.37	130	339	39.0	6.82	61.3	260	7.29
LC-01-19	98.5	0.220	0.021	0.760	0.0130	24.5	22.7	1.15	10.2	75.1	2.30	40.2	412	76.9	2.02	114	2649	17.0
LC-01-20	98.7	0.400	0.031	0.770	0.0110	62.4	64.8	0.930	10.1	77.2	3.61	46.6	75.3	60.2	2.08	9.70	18.1	5.52
LC-01-21	98.3	0.490	0.019	0.970	0.0190	180	309	3.31	9.88	74.5	7.47	96.8	113	78.7	4.88	11.9	58.7	8.28
LC-01-22	98.2	0.510	0.022	1.03	0.0670	78.7	67.9	0.670	10.0	75.1	5.86	85.7	424	54.7	4.73	128	251	10.8
LC-01-23	81.8	1.340	0.042	11.7	3.7600	52.0	69.8	9.62	8.91	63.1	12.0	55.5	239	50.8	2.82	39.3	316	6.05
LC-01-24	98.4	0.400	0.050	0.940	0.0740	65.7	69.2	0.490	10.7	76.4	4.25	55.5	114	57.3	2.62	11.9	35.0	5.62
LC-01-25	98.9	0.300	0.015	0.630	0.0100	177	385	1.75	10.6	77.7	3.83	134	67.2	29.0	7.31	24.1	25.7	4.10
LC-01-26	98.3	0.180	0.023	0.980	0.0810	16.8	19.0	—	9.85	75.7	1.41	37.5	158	63.7	1.78	15.6	2357	11.8
LC-01-27	98.7	0.400	0.023	0.650	0.0170	90.4	141	4.17	10.3	77.9	4.66	85.7	442	58.9	5.08	107	290	8.74
LC-01-28	98.3	0.270	0.022	0.740	0.0250	35.7	33.1	1.27	10.2	72.8	3.23	39.6	483	128	2.10	69.1	3783	17.7
LC-01-29	98.8	0.320	0.014	0.810	0.0078	41.7	43.3	2.34	10.0	79.0	3.02	50.2	32.8	33.6	1.87	1.45	12.6	3.65
LC-01-30	98.9	0.290	0.023	0.750	0.0074	41.7	41.6	—	10.7	76.1	2.63	59.9	35.6	29.1	2.17	2.84	16.9	3.37
LC-01-31	98.9	0.098	0.010	0.780	0.0046	9.43	12.5	1.75	10.3	77.6	0.770	40.7	265	27.6	2.28	72.0	912	5.40
LC-01-32	98.2	0.270	0.024	0.850	0.0270	33.3	36.4	0.440	10.3	78.4	3.78	47.3	661	80.3	2.00	55.4	3180	35.7
LC-01-33	98.9	0.140	0.007	0.720	0.0081	13.6	15.4	—	10.7	79.7	1.52	36.6	150	43.7	1.46	40.8	1295	8.10
LC-01-34	98.9	0.110	0.009	0.730	0.0055	11.2	15.2	1.70	10.7	76.9	1.07	38.7	207	29.0	2.17	82.8	991	5.45
LC-02-01	97.0	0.730	0.340	0.780	0.0240	144	440	6.74	10.5	73.9	6.38	101	170	229	3.73	2.73	7366	58.2
LC-02-02	98.3	0.091	0.430	0.690	0.0084	13.2	30.5	5.72	10.2	76.9	1.76	54.6	78.0	27.3	1.98	6.56	3209	15.7
LC-02-03	98.1	0.100	0.440	0.790	0.0057	13.6	30.1	0.04	10.3	74.2	2.25	59.7	56.8	22.0	1.71	2.59	4147	19.1
LC-02-04	97.5	0.230	0.220	1.14	0.0700	45.4	85.3	0.440	9.94	76.8	6.09	30.8	138	43.5	1.00	3.29	5796	15.7
LC-02-05	97.5	0.400	0.100	0.860	0.0340	27.7	148	1.98	10.4	75.2	6.74	15.4	8.27	84.7	0.27	0.017	7676	26.9
LC-02-06	98.3	0.670	0.160	0.580	0.0320	111	723	2.87	10.2	74.4	12.0	56.6	4.73	71.6	1.68	0.14	337	13.1
LC-02-07	98.4	0.130	0.290	0.700	0.0130	20.3	38.0	0.950	10.3	74.8	1.51	30.8	68.8	26.1	0.82	1.58	3325	12.1
LC-02-08	98.1	0.093	0.400	0.830	0.0080	21.9	32.9	0.10	10.6	72.5	2.10	34.9	71.7	22.5	1.03	2.47	3800	19.3
LC-02-09	96.0	1.250	0.910	1.15	0.2000	380	530	4.65	10.3	74.1	13.3	483	268	94.6	24.4	28.1	194	40.2
LC-02-10	98.8	0.038	0.280	0.750	0.0004	34.2	45.2	—	10.9	76.5	0.420	78.1	433	4.31	4.82	26.3	54.3	3.17
LC-02-11	98.2	0.160	0.250	0.850	0.0230	28.2	77.4	0.740	11.0	72.4	2.45	51.9	98.7	32.1	2.14	4.11	3371	11.8
LC-02-12	96.3	0.700	1.53	0.790	0.0140	121	510	25.70	9.91	73.7	6.59	207	235	118	12.3	18.6	3029	67.8
LC-02-13	97.3	0.280	0.880	0.690	0.0230	32.2	108	4.73	10.7	75.2	3.42	81.1	162	34.9	4.12	30.1	6071	25.4
LC-02-14	98.5	0.520	0.094	0.740	0.0074	19.3	35.2	—	10.5	74.7	1.76	100	91.9	48.5	3.63	6.54	16.4	8.82
LC-02-15	97.4	0.740	0.043	0.800	0.0270	22.7	65.1	—	10.2	77.6	9.08	49.9	2.12	127	1.01	0.0081	6964	39.8
LC-02-16	98.4	0.170	0.480	0.770	0.0120	39.6	121	1.73	10.4	77.7	3.29	55.9	32.0	22.6	1.83	1.03	808	8.27
LC-02-17	98.6	0.300	0.160	0.730	0.0190	118	509	4.24	10.2	75.6	6.88	82.1	2.24	25.8	2.61	0.076	26.1	5.34
LC-02-18	98.3	0.840	0.024	0.670	0.0200	63.1	111	1.89	10.6	73.8	9.53	17.3	30.9	150	0.22	0.030	111	25.9
LC-02-19	91.9	1.220	0.540	5.88	0.1700	141	331	—	9.79	69.5	23.5	56.6	14.9	145	1.42	0.500	660	30.0
LC-02-20	98.1	0.770	0.180	0.770	0.0690	53.7	215	—	10.1	74.8	23.7	47.8	3.29	72.9	1.30	0.047	362	11.7
LC-02-21	97.3	1.170	0.380	0.860	0.0190	143	648	3.03	10.1	73.8	8.97	69.3	27.8	188	2.62	1.19	158	33.8
LC-02-22	98.2	0.780	0.022	0.870	0.0180	42.9	87.0	0.790	10.0	73.5	7.64	28.0	15.1	117	0.61	0.034	70.7	18.2
LC-02-24	96.8	0.960	1.22	0.780	0.0170	131	484	6.37	10.5	71.3	9.31	187	129	68.3	8.54	8.40	183	31.6
LC-02-25	98.3	0.100	0.300	0.850	0.0098	15.7	52.1	—	10.6	75.9	1.13	46.1	62.2	10.5	1.28	0.730	3127	8.54
LC-02-26	98.5	0.330	0.420	0.640	0.0160	112	216	3.34	10.3	71.4	4.37	38.1	18.1	21.2	0.97	0.420	133	7.24
LC-02-27	97.0	1.110	0.860	0.750	0.0320	242	725	25.30	9.86	72.2	11.1	159	42.1	62.8	9.85	5.32	37.0	27.7
Oxidized type																		
SK-04-01	99.1	0.250	0.500	0.130	0.0230	1.35	87.0	4.36	10.8	78.9	23.8	17.7	0.790	3.24	0.36	0.029	12.4	3.26
SK-04-03	99.7	0.049	0.120	0.130	0.0014	34.0	37.4	—	10.9	79.9	2.77	50.6	25.2	0.33	1.79	3.19	9.7	0.430
SK-04-04	99.1	0.033	0.045	0.140	0.0012	0.380	1.12	0.320	10.8	76.8	2.86	13.9	1.93	4.11	0.42	0.0054	5122	7.05
SK-04-05	99.4	0.150	0.150	0.140	0.0052	11.0	20.1	4.13	10.3	79.5	12.2	30.4	0.780	3.69	0.88	0.011	796	5.17
SK-04-06	98.5	0.068	0.230	0.081	0.0044	1.90	4.07	0.350	10.1	76.9	10.9	6.34	5.25	9.8	0.12	0.011	8510	20.8
SK-04-07	99.7	0.094	0.070	0.130	0.0106	0.50	21.8	7.71	10.8	79.7	8.53	14.9	0.130	0.78	0.58	0.018	10.6	0.310
SK-04-08	99.6	0.150	0.033	0.140	0.0049	2.11	7.59	1.98	10.9	79.5	16.6	4.37	0.600	5.33	0.18	0.011	473	2.50
SK-04-09	98.1	0.069	0.780	0.130	0.0015	2.49	26.2	15.5	10.9	75.9	11.1	24.3	39.5	10.1	0.39	0.100	7383	30.7
SK-04-10	99.0	0.600	0.230	0.120	0.0150	16.2	38.8	9.27	10.7	78.8	70.5	11.4	1.04	13.1	0.24	0.010	81.2	8.37
SK-04-11	98.2	0.065	0.690	0.120	0.0022	3.67	25.0	8.97	10.1	75.3	27.2	22.3	36.8	13.4	0.51	0.110	6965	30.4
SK-04-12	99.7	0.026	0.069	0.140	0.0004	12.0	114	0.440	10.8	79.5	1.64	11.4	0.460	0.45	0.34	0.0075	4.43	0.460
SK-04-13	99.2	0.100	0.009	0.120	0.0130	0.490	4.18	0.690	10.5	79.1	4.94	0.920	0.410	37.6	0.075	0.016	3841	8.14
SK-04-14	99.6	0.009	0.200	0.140	0.0001	1.42	97.5	83.7	10.7	77.6	0.430	84.3	7.50	0.74	4.56	2.19	205	0.470
SK-04-15	99.6	0.036	0.010	0.120	0.0015	0.03	0.620	0.960	10.3	78.2	26.1	0.67	0.110	25.3	0.022	0.013	1477	12.4
SK-05-03	98.6	0.500	0.570	0.120	0.0120	2.55	822	94.2	10.2	75.4	65.4	64.7	19.8	12.0	1.98	0.500	5.71	11.0
SK-05-04	99.1	0.240	0.400	0.130	0.0084	0.680	454	39.3	10.3	81.1	35.4	53.6	14.3	25.3	1.53	0.140	142	26.0
SK-05-06	99.2	0.580	0.034	0.140	0.0170	0.320	39.0	1.40	10.6	75.3	75.9	7.13	0.340	26.3	0.11	0.0082	35.7	8.32
SK-05-07	99.3	0.400	0.038	0.130	0.0052	0.180	28.2	2.65	10.2	76.9	54.9	8.60	1.07	16.6	0.26	0.0057	501	6.68
SK-05-11	99.3	0.460	0.003	0.150	0.0120	0.077	1.85	3.63	10.3	78.6	87.6	9.80	0.00470	15.3	0.27	0.0027	0.74	4.80
SK-05-12	99.8	0.006	0.004	0.160	0.0003	0.004	1.53	2.13	10.4	76.1	1.16	0.750	0.0490	12.1	0.016	0.0028	178	11.6
SK-05-17	99.1	0.014	0.590	0.150	0.0007	0.540	65.0	61.2	10.7	78.2	2.62	156	23.5	26.5	4.25	0.230	253	22.7
SK-05-18	99.6	0.110	0.120	0.140	0.0042	10.7	36.9	5.35	9.89	75.7	12.2	14.5	0.490	2.47	0.35	0.009	22.0	0.690
SK-05-19	99.1	0.540	0.170	0.130	0.0030	40.6	115	—	10.2	75.7	72.8	16.5	2.05	10.2	0.40	0.090	121	10.2

"—" represent below detection limit.

LA–ICP–MS mapping enabled a suite of trace elements to be simultaneously measured across the surface of the cassiterites. It is therefore a powerful tool for understanding the relationship between chemical composition and color variations. Trace element mapping results show a significant relationship between element distribution and CL-defined zoning in all cassiterite grains. The distribution of Nb, Ta, and Ti, revealed by elemental mapping (Figure 6), correlates with the regular oscillatory zoning pattern displayed by CL images. Dark luminescing domains of these cassiterite grains often showed relatively high Sb, Fe, W, Ga, and U, and low Nb and Ta [8,44]. In this study, we discuss skarn (KF–05), and massive sulfide samples (LC–01) in detail as examples. In elemental maps of the cassiterite grain

from skarn ores (see Figure 6a), the dark luminescing domains reveal high Nb, Ta, W, and U contents. The regular oscillatory zoning pattern correlates with the distribution of Nb, Ta, and Ti. However, in elemental maps of the cassiterite grain from massive sulfide ores (see Figure 6b), dark luminescing domains reveal high Sb, W, and U contents. The regular oscillatory zoning pattern correlates with the distribution of Nb, Ta, and Ti. In summary, the dark luminescing domains of cassiterite grains from the Gejiu tin polymetallic deposit are mainly related with the concentrations of U and W. Comparatively, the regular oscillatory zoning pattern mainly correlates with the distribution of Nb, Ta, and Ti.
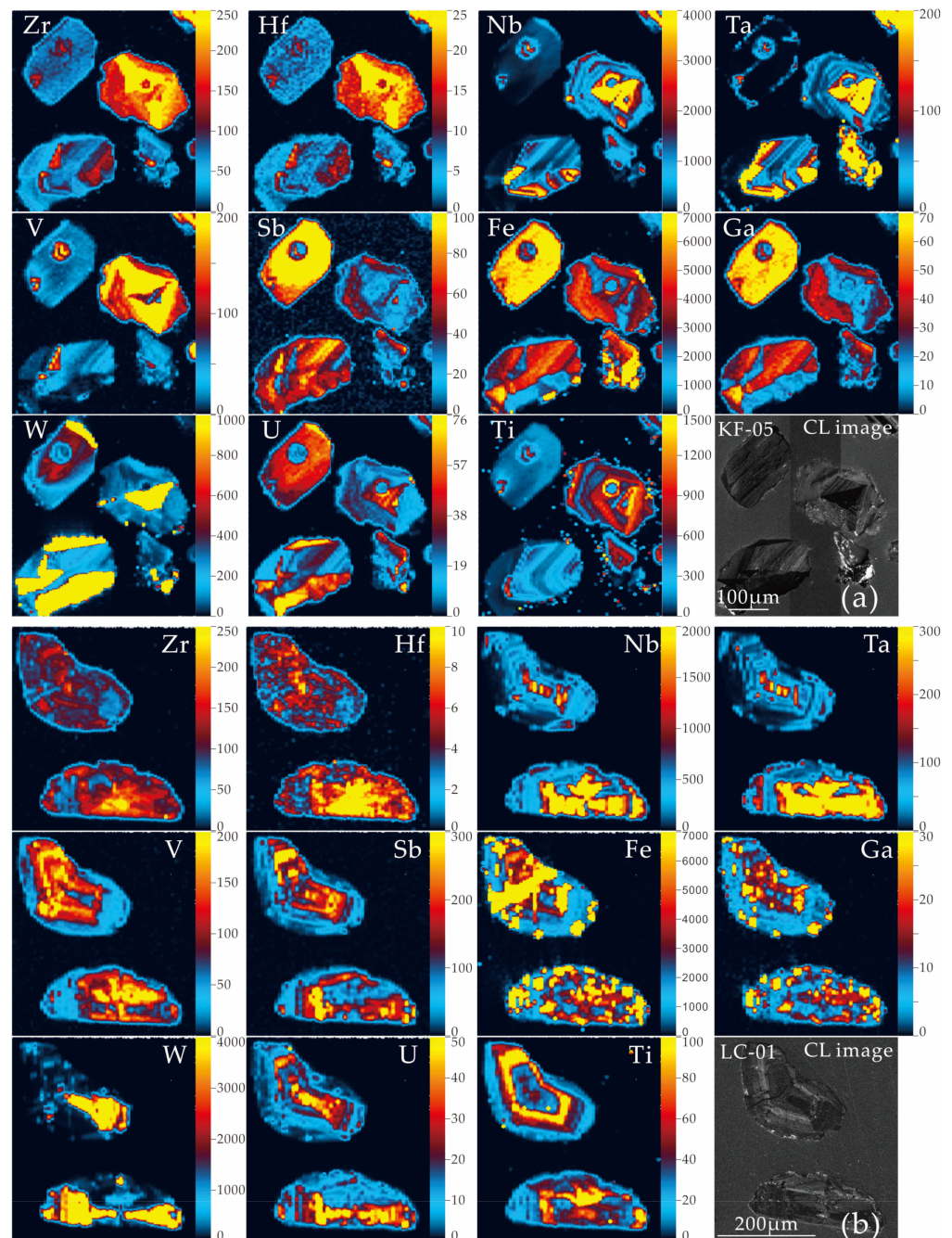
Figure 6. Coupled cathodoluminescence (CL) images and LA–ICP–MS multiple elemental mapping results of cassiterite from tin-granite (**a**), massive sulfide (**b**).

6. Discussion

6.1. Chronology of the Gejiu Tin Polymetallic Deposit

There is a wide range of views on ages of mineralization in the Gejiu tin polymetallic deposit. Qin et al. [20] used K–Ar and ^{40}Ar–^{39}Ar dating on quartz/cassiterite and Pb–Pb dating on sulfide to argue for a broad mineralization age from 83.23 ± 2.07 to ~240 Ma. Yang et al. [21] performed Re–Os dating of molybdenite from the Kafang skarn Cu–Sn deposit, one of the four ore fields in the Gejiu tin polymetallic deposit, and obtained an isochron age of 83.4 ± 2.1 Ma. The ^{40}Ar–^{39}Ar dating of muscovite from the muscovite–tourmaline–quartz vein ores in Laochang yielded a plateau age of 82.7 ± 0.7 Ma, which was considered as the mineralization age of the tin polymetallic deposit [45]. Li et al. [46] interpreted a cassiterite ^{40}Ar–^{39}Ar isochron age of 206.8 ± 3.2 Ma and a ^{40}Ar–^{39}Ar plateau age of 202.2 ± 2.4 Ma from the Lutangba orebody as the tin mineralization ages. Zhao et al. [10] collected two types of cassiterite from the Xi'ao Cu–Sn polymetallic deposit and acquired cassiterite U–Pb ages of 83.3 ± 2.1 and 84.9 ± 1.7 Ma, which are similar to the mineralization ages of the Gaosong Sn–Cu deposit (cassiterite U–Pb age of 83.5 ± 2.1–85.1 ± 1.0 Ma, after Guo et al. [8]). Of the various ages above derived from different methods, we prefer cassiterite U–Pb ages, which can be used directly to constrain the tin mineralization event [1,3,11,13,14,17,47] as the mineralization timing. The result of cassiterite U–Pb dating in the present study shows that Sn mineralization timing of the Gejiu tin polymetallic deposit falls within a narrow range of 83.4 ± 0.64 to 87.0 ± 1.6 Ma, in agreement with previously published cassiterite U–Pb ages of 76.4 ± 1.7 to 85.1 ± 1.0 Ma within their respective analytical uncertainties [3,8,10,22]. This indicates that tin mineralization occurred in the Late Cretaceous period within a relatively short time, suggesting that hydrothermal tin mineralization duration was short.

We note that no Triassic cassiterite U–Pb age has been reported up until now. This is contrary to the model proposed by Qin et al. [20,48], who argued that the stratiform-like tin mineralization of Triassic submarine exhalative sedimentary (SEDEX) origin had been modified by Cretaceous magmatic activity [23,34,46,49,50]. Given the age data presented here, this model may not be reasonable for the genesis of the Gejiu tin polymetallic deposit. Instead, our cassiterite U–Pb ages coincide with the mica ^{40}Ar–^{39}Ar plateau ages (85.6 ± 0.7 Ma for the stratiform-like weathered ore and 84.3 ± 0.6 Ma for the skarn ore [28]) and zircon U–Pb ages of 77.4 ± 2.5 ~ 85.8 ± 0.6 Ma for the granitic pluton [30–33,51]. These ages suggest there is a close temporal and genetic relationship between Late Cretaceous granitic magmatism and tin mineralization in the Gejiu district. This viewpoint is consistent with the magmatic–hydrothermal model proposed by others [8,10,22,24,25,28,30–33,35,52,53]. The chemical composition of hydrothermal cassiterite can be a sensitive indicator for the mineralization type [54–56]. Enrichment of W in cassiterite from granite-related deposits and the limited Fe content in cassiterites from VMS/SEDEX deposits [55] are two key discriminating factors for determining genesis [8,55]. Almost all cassiterites in this study are characterized by high W and Fe contents and plot in the granite-related tin deposit area (Figure 7a), further suggesting that Gejiu tin polymetallic deposit is of magmatic–hydrothermal origin. This genetic model is supported by H–O stable isotopic composition of cassiterites ($\delta^{18}D_{H2O-SMOW}$ = −79−−153‰, $\delta^{18}O_{H2O-SMOW}$ = 7.16–8.25‰) coinciding with those of fluids derived from magmatic hydrothermal systems in available data [10,12,25,57].
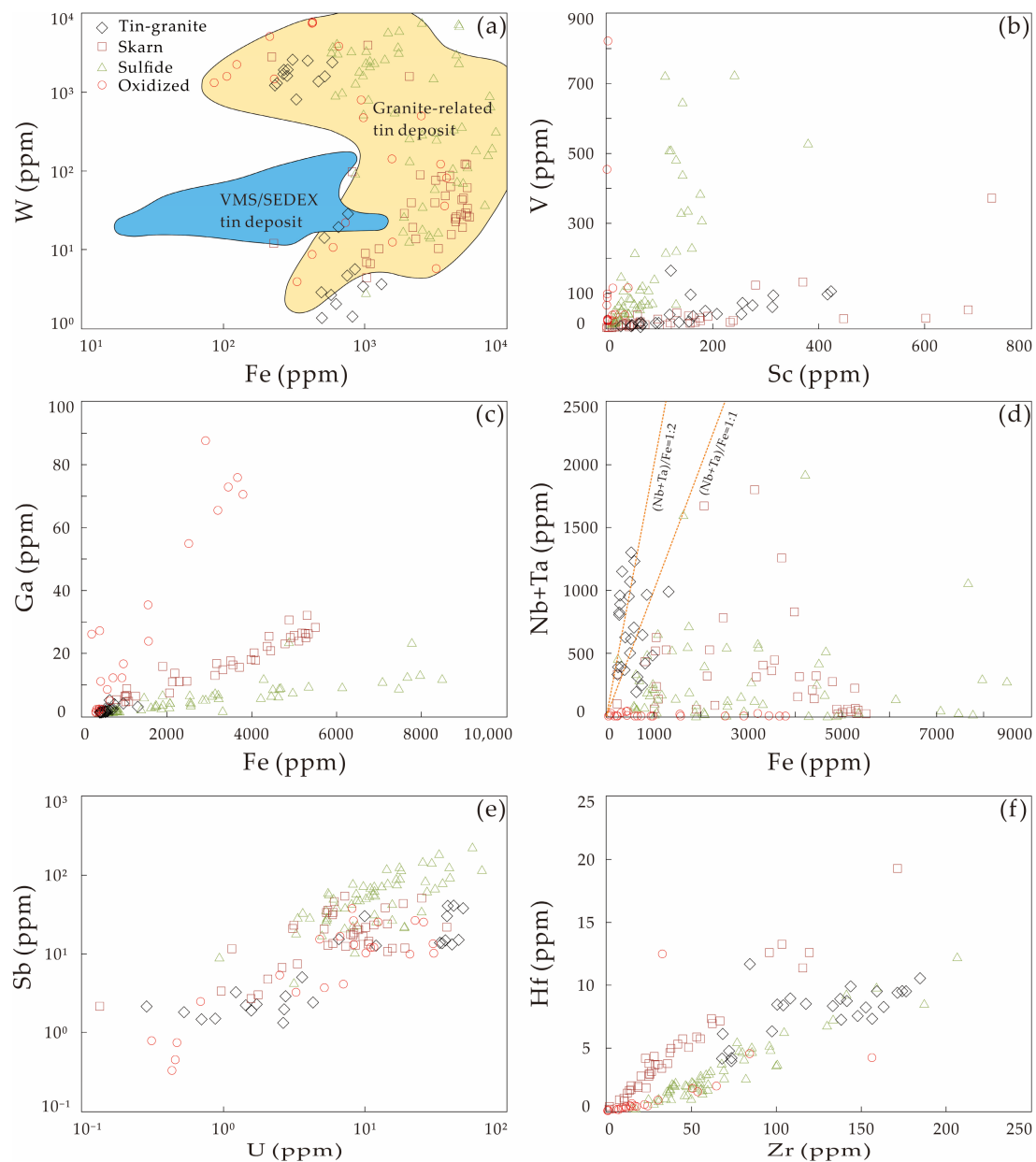
Figure 7. Correlation binary plots of selected trace elements in cassiterite samples from the Gejiu tin polymetallic deposit. (**a**) The plot of W vs. Fe displays that the tin mineralization is related to granitic magmatism; (**b**,**c**) The plots of V vs. Sc and Ga vs. Fe display a clear positive correlation; (**d**) The plot of Nb+Ta vs. Fe displays cassiterite from tin-granite have a (Nb + Ta)/Fe ratio near 1; (**e**,**f**) The plots of Sb vs. U and Hf vs. Zr display a positive correlation.

6.2. The Elemental Substitution Mechanism and Precipitation Environment of Cassiterites: Insights from Multiple Element Mapping and Trace Element Variations

Systematic variations in the chemical composition of cassiterite and substitution mechanisms are interpreted to be related to ore-forming environments and physicochemical conditions [5,54,56,58]. Considering the charge and radius of ions, cations such as Fe^{3+}, Ga^{3+}, Al^{3+}, Sc^{3+}, Sb^{3+}, W^{4+}, U^{4+}, Zr^{4+}, Hf^{4+}, Ti^{4+}, V^{5+}, Nb^{5+}, and Ta^{5+} are considered compatible in cassiterite [59,60]. This is evidenced by high concentrations of these elements in cassiterite presented in previous studies [3,5,54,56,61]. Most of these compatible elements in the cassiterite samples examined here are in appreciable quantities and have significant compositional differences between different ore-type samples. These variations can provide indicative information on elemental substitution mechanisms in cassiterites.

Previously, elevated total Fe, Nb, Ta, Ti, Sc, and Mn contents were considered to play an important role in controlling color variation revealed by CL images of cassiterites [3,7,8,62]. Elemental mapping of cassiterite grains presented here indicates that the dark luminescing domains in CL are mainly related with elevated W and U as described above, whereas high concentrations of Ti and Mn are not necessary. Elemental maps further revealed the regular oscillatory zoning patterns mainly correlate with the distribution of Nb, Ta, and Ti (Figure 6a,b).

Elemental binary diagrams show a clear positive correlation between Sc and V (Figure 7b) and between Fe and Ga (Figure 7c) in the cassiterite samples analyzed here. Because Sc only has a single valence state (+3) under geological conditions [3], the positive Sc–V correlation indicates that V in the 5^+ valence state incorporates in the cassiterite lattice, allowing a charge-balanced coupled substitution of $Sc^{3+} + V^{5+} \leftrightarrow 2 (Sn, Ti)^{4+}$. Similarly, the significant correlation between Fe and Ga (Figure 7c) could be interpreted as the coupled substitution of $Fe^{3+} + Ga^{5+} \leftrightarrow 2 (Sn, Ti)^{4+}$. However, the apparent higher content of Fe than that of Ga indicates that the incorporation of Fe might also follow another substitution: $Fe^{3+} + OH^- \leftrightarrow Sn^{4+} + O^{2-}$ or $Fe^{3+} + H^+ \leftrightarrow Sn^{4+}$ [54,63].

As valence state directly impacts the compatibility of an element in cassiterite [3,7], some redox sensitive elements such as W (+4 or +6), U (+4 or +6), Fe (+2 or +3), or Sb (+3 or +5) can be used as a powerful probe for evaluating the redox conditions of mineral precipitation processes. The distinct concentration variations of these elements in different domains of cassiterites are interpreted to reflect redox-driven chemical modification by reaction with hydrothermal fluid [3,7]. Combining the internal texture with the distribution and concentration of redox-sensitive elements in cassiterites, we can speculate on changes in redox and fluid mixing or reaction, which are considered as the most important drivers for the precipitation of tin ore [64]. Thus, this approach may be especially useful for understanding Sn mineralization systems [3]. There are two ideal coupled substitutions for incorporation of Nb and Ta in cassiterite: (1) $Fe^{2+} + 2(Nb, Ta)^{5+} \leftrightarrow 3 (Sn, Ti)^{4+}$ ((Nb + Ta)/Fe $\approx$ 2) under a reduced condition; (2) $Fe^{3+} + (Nb, Ta)^{5+} \leftrightarrow 2 (Sn, Ti)^{4+}$ ((Nb + Ta)/Fe $\approx$ 1) under an oxidized state [3,54,64–66], because isomorphous replacement of Sn_3O_6 by $(Fe,Mn)(Nb,Ta)_2O_6$ is typical of cassiterite in hydrothermal Sn deposits [54,56]. The incorporation of Nb and Ta depend greatly on the Fe valence, and consequently on the redox condition in the system. We can therefore define which substitution occurred in the cassiterite precipitation process according to the ratio of mol (Nb + Ta)/Fe. Only tin-granite cassiterite reveals (Nb + Ta)/Fe near 1 (Figure 7d), suggesting that tin-granite cassiterite was formed under an oxidized state with substitution (2) above. For magmatic–hydrothermal cassiterites from skarn, massive sulfide, and oxidized-type ores, there could be a more complex substitution mechanism, such as substitutions of $Fe^{3+} + OH^- \leftrightarrow Sn^{4+} + O^{2-}$ and $Fe^{3+} + H^+ \leftrightarrow Sn^{4+}$ (oxidizing environment) as proposed by previous studies [54,63,66,67]. However, under oxidized conditions, U exists in 5+ or 6+ state and is therefore incompatible in cassiterite, but is fluid mobile and transported out of the cassiterite [3,4,68]. The relatively elevated U and Sb contents and positive correlation (Figure 7e) suggest that these cassiterites were precipitated under a reduced environment, where Sb^{3+} and U^{4+} are more compatible than Sb^{5+} and U^{5+} (or U^{6+}). Zr and Hf have similar geochemical behavior, so they usually are constant in Zr/Hf ratio of 35–40 [69]. However, element pair decoupling can occur in hydrothermal environments and in highly differentiated igneous rocks [70–73]. Processes such as metasomatism, hydrothermal alteration, or preferential mobilization of Zr in B-rich and F-rich fluids have been proposed to cause fractionation of Zr over Hf [3,65]. Cassiterite samples studied here show a wide variation of Zr/Hf ratio (5–78, see Figure 7f), agreeing with the high activity of B and F during the Sn mineralization in Gejiu. This is also proved by the abundant tourmaline ($NaR_3Al_6Si_6O_{18}BO_{33}(OH,F)_4$) and fluorite ($CaF_2$) in ores reported in previous literature [3,8,10,22].

7. Conclusions

(1) Cassiterite U–Pb ages at around 85 Ma coincides with the crystallization ages of Late Cretaceous granitoids in the Gejiu district, suggesting that there is a temporal and spatial genetic relationship between Late Cretaceous granitic magmatism and tin mineralization.

(2) The distribution of Nb, Ta, and Ti in cassiterite grains correlate with regular oscillatory zoning patterns displayed by CL images. Comparatively, relatively high Sb, W, and U concentrations correlate with the dark luminescing domains in cassiterite grains.

(3) The variation relevance of redox sensitive elements such as W, U, Fe, and Sb suggest that tin-granite cassiterite was formed under an oxidized state whereas skarn, massive sulfide, and oxidized cassiterites were precipitated in a reduced environment.

Author Contributions: Data curation, S.T.; formal analysis, X.H.; funding acquisition, S.T. and X.H.; investigation, X.H., C.B., Y.L. and Z.L.; resources, S.T.; software, X.H.; supervision, S.T.; writing—original draft, X.H.; writing—review and editing, X.H. and N.L. All authors have read and agreed to the published version of the manuscript.

Data Availability Statement: The data presented in this study are available in this article.

References

1. Li, C.Y.; Zhang, R.Q.; Ding, X.; Ling, M.X.; Fan, W.M.; Sun, W.D. Dating cassiterite using laser ablation ICP–MS. *Ore Geol. Rev.* **2016**, *72*, 313–322. [CrossRef]
2. Carr, P.C.; Norman, M.D.; Bennett, V.G. Assessment of crystallographic orientation effects on secondary ion mass spectrometry (SIMS) analysis of cassiterite. *Chem. Geol.* **2017**, *467*, 122–133. [CrossRef]
3. Cheng, Y.B.; Spandler, C.; Kemp, A.; Mao, J.W.; Rusk, B.; Hu, Y.; Blake, K. Controls on cassiterite (SnO_2) crystallization: Evidence from cathodoluminescence, trace–element chemistry, and geochronology at the Gejiu Tin District. *Am. Mineral.* **2019**, *104*, 118–129. [CrossRef]
4. Gemmrich, L.; Lisard, T.; Melgarejo, J.C.; Laurent, O.; Vallance, J.; Chelle–Michou, C.; Sempere, T.P.A. Trace element composition and U–Pb ages of cassiterite from the Bolivian tin belt. *Miner. Depos.* **2021**, *3*, 1–30. [CrossRef]
5. Plimer, I.R.; Lu, J.; Kleeman, J.D. Trace and rare earth elements in cassiterite–sources of components for the tin deposits of the Mole Granite, Australia. *Miner. Depos.* **1991**, *26*, 267–274. [CrossRef]
6. Jiang, S.Y.; Yu, J.M.; Lu, J.J. Trace and rare–earth element geochemistry in tourmaline and cassiterite from the Yunlong tin deposit, Yunnan, China: Implication for migmatitic–hydrothermal fluid evolution and ore genesis. *Chem. Geol.* **2004**, *209*, 193–213. [CrossRef]
7. Lerouge, C.; Gloaguen, E.; Wille, G.; Bailly, L. Distribution of In and other rare metals in cassiterite and associated minerals in Sn ±W ore deposits of the western Variscan Belt. *Eur. J. Mineral.* **2017**, *29*, 739–753. [CrossRef]
8. Guo, J.; Zhang, R.Q.; Li, C.Y.; Sun, W.D.; Hu, Y.B.; Kang, D.M.; Wu, J.D. Genesis of the Gaosong Sn–Cu deposit, Gejiu district, SW China: Constraints from in situ LA–ICP–MS cassiterite U–Pb dating and trace element fingerprinting. *Ore Geol. Rev.* **2018**, *92*, 627–642. [CrossRef]
9. Guo, J.; Zhang, R.Q.; Sun, W.D.; Ling, M.X.; Hu, Y.B.; Wu, K.; Luo, M.; Zhang, L.C. Genesis of tin–dominant polymetallic deposits in the Dachang district, South China: Insights from cassiterite U–Pb ages and trace element compositions. *Ore Geol. Rev.* **2018**, *95*, 863–879. [CrossRef]
10. Zhao, Y.H.; Chen, S.Y.; Huang, Y.Q.; Zhao, J.N.; Tong, X.; Chen, X.S. U–Pb ages, O isotope compositions, raman spectrum, and geochemistry of cassiterites from the Xi'ao copper–tin polymetallic deposit in Gejiu district, Yunnan province. *Minerals* **2019**, *9*, 212. [CrossRef]
11. Gulson, B.L.; Jones, M.T. Cassiterite: Potential for direct dating of mineral deposits and a precise age for the Bushveld complex granites. *Geology* **1992**, *20*, 355–358. [CrossRef]
12. Liu, Y.P.; Li, Z.X.; Li, H.M.; Guo, L.G.; Xu, W.; Ye, L.; Li, C.Y.; Pi, D.H. U–Pb geochronology of cassiterite and zircon from the Dulong Sn–Zn deposit: Evidence for Cretaceous large–scale granitic magmatism and mineralization events in southeastern Yunnan province, China. *Acta Petrol. Sin.* **2007**, *23*, 967–976. (In Chinese)
13. Yuan, S.D.; Peng, J.T.; Hu, R.Z.; Li, H.M.; Shen, N.P.; Zhang, D.L. A precise U–Pb age on cassiterite from the Xianghualing tin–polymetallic deposit (Hunan, south China). *Miner. Depos.* **2008**, *43*, 375–382. [CrossRef]

14. Yuan, S.D.; Peng, J.T.; Hao, S.; Li, H.M.; Geng, J.Z.; Zhang, D.L. In situ LA–MC–ICP–MS and ID–TIMS U–Pb geochronology of cassiterite in the giant Furong tin deposit, Hunan Province, South China: New constraints on the timing of tin–polymetallic mineralization. *Ore Geol. Rev.* **2011**, *43*, 235–242. [CrossRef]

15. Zhang, D.L.; Peng, J.T.; Hu, R.Z.; Yuan, S.D.; Zheng, D.S. The closure of U–Pb system in cassiterite and its reliability for dating. *Geol. Rev.* **2011**, *57*, 549–554. (In Chinese)

16. Legros, H.; Harlaux, M.; Mercadier, J.; Romer, R.L.; Poujol, M.; Camacho, A.; Marignac, C.; Cuney, M.; Wang, R.C.; Charles, N.; et al. The world–class Nanling metallogenic belt (Jiangxi, China): W and Sn deposition at 160 Ma followed by 30 m.y. of hydrothermal metal redistribution. *Ore Geol. Rev.* **2020**, *117*, 103–302. [CrossRef]

17. Zhang, R.Q.; Lehmann, B.; Seltmann, R.; Sun, W.D.; Li, C.Y. Cassiterite U–Pb geochronology constrains magmatic–hydrothermal evolution in complex evolved granite systems: The classic Erzgebirge tin province (Saxony and Bohemia). *Geology* **2017**, *45*, 1095–1098. [CrossRef]

18. 308 Geological Party. *Geology of Tin Deposit in Gejiu Area*; Metallurgical Industry Publishing House: Beijing, China, 1984; p. 236. (In Chinese)

19. Zhuang, Y.Q.; Wang, R.Z.; Yang, S.P.; Yi, J.M. *Tin–Copper Polymetallic Deposits in Gejiu District*; Earthquake Publishing House: Beijing, China, 1996; pp. 1–189. (In Chinese)

20. Qin, D.X.; Li, Y.S.; Tan, S.C.; Chen, A.B.; Xue, C.D.; Fan, Z.G.; Dang, Y.T.; Tong, X.; Wu, J.D.; Li, Y.X.; et al. Metallogenic ages of Gejiu tin ore deposit in Yunnan Province. *Chin. J. Geol.* **2006**, *44*, 122–132. (In Chinese)

21. Yang, Z.X.; Mao, J.W.; Chen, M.H.; Tong, X.; Wu, J.D.; Cheng, Y.B.; Zhao, H.J. Re–Os dating of molybdenite from the Kafang skarn copper (tin) deposit in the Gejiu tin polymetallic ore district and its geological significance. *Acta Petrol. Sin.* **2008**, *24*, 1937–1944. (In Chinese)

22. Zhang, Y.H.; Zhou, J.X.; Tan, S.C.; Li, H.M.; Hao, S.; Jiang, Y.G.; He, X.H. Genesis of the oxidized Sn ores in the Gejiu district, Yunnan Province, SW China. *Ore Geol. Rev.* **2020**, *121*, 103474. [CrossRef]

23. Zhang, H.; Gao, Z.M.; Ma, D.Y.; Tao, Y.; Liu, H. Distribution and genetic significance of Sn in oolitic pyrite and colloidally structure pyrite from Gejiu tin deposits. *Acta Mineral. Sin.* **2004**, *24*, 87–91. (In Chinese)

24. Zhang, J.; Mao, J.W.; Cheng, Y.B.; Li, X.L. Mineralization process of the Kafang tin–copper deposit in the Gejiu district, Yunnan province: Constraints from fluid inclusion. *Acta Petrol. Sin.* **2012**, *28*, 166–182. (In Chinese)

25. Liao, S.L.; Chen, S.Y.; Deng, X.H.; Li, P.; Zhao, J.N.; Liao, R.Y.Z. Fluid inclusion characteristics and geological significance of the Xi'ao copper–tin polymetallic deposit in Gejiu, Yunnan Province. *J. Asian Earth Sci.* **2014**, *79*, 455–467. [CrossRef]

26. Mao, J.W.; Cheng, Y.B.; Guo, C.L.; Yang, Z.X.; Zhao, H.J. Gejiu tin polymetallic ore–field: Deposit model and discussion. *Acta Geol. Sin.* **2008**, *81*, 1456–1468. (In Chinese)

27. Cheng, Y.B.; Mao, J.W.; Chang, Z.; Pirajno, F. The origin of the world class tin–polymetallic deposits in the Gejiu district, SW China: Constraints from metal zoning characteristics and ^{40}Ar–^{39}Ar geochronology. *Ore Geol. Rev.* **2013**, *53*, 50–62. [CrossRef]

28. Zhang, J.W.; Dai, C.G.; Huang, Z.L.; Luo, T.Y.; Qian, Z.K.; Zhang, Y. Age and petrogenesis of Anisian magnesian alkali basalts and their genetic association with the Kafang stratiform Cu deposit in the Gejiu supergiant tin–polymetallic district, SW China. *Ore Geol. Rev.* **2015**, *69*, 403–416. [CrossRef]

29. Cheng, Y.B.; Mao, J.W.; Rusk, B.; Yang, Z.X. Geology and genesis of Kafang Cu–Sn deposit, Gejiu district, SW China. *Ore Geol. Rev.* **2012**, *48*, 180–196. [CrossRef]

30. Cheng, Y.B.; Mao, J.W.; Spandler, C. Petrogenesis and geodynamic implications of the Gejiu igneous complex in the western Cathaysia block, South China. *Lithos* **2013**, *175–176*, 213–229. [CrossRef]

31. Wang, Q.; Li, J.W.; Jian, P.; Zhao, Z.H.; Xiong, X.L.; Bao, Z.W.; Xu, J.F.; Li, C.F.; Ma, J.L. Alkaline syenites in eastern Cathaysia (South China): Link to Permian–Triassic transtension. *Earth Planet. Sci. Lett.* **2005**, *230*, 339–354. [CrossRef]

32. Li, X.L.; Mao, J.W.; Chen, Y.B.; Zhang, J. Petrogenesis of the Gaofengshan granite in Gejiu area, Yunnan Province Zircon U–Pb dating and geochemical constraints. *Acta Petrol. Sin.* **2012**, *28*, 183–198. (In Chinese)

33. Cheng, Y.B.; Mao, J.W. Age and geochemistry of granites in Gejiu area, Yunnan province, SW China: Constraints on their petrogenesis and tectonic setting. *Lithos* **2010**, *120*, 258–276.

34. Qian, Z.K.; Luo, T.Y.; Huang, Z.L.; Tong, X.; Yang, B.F.; Yang, W.B.; Lu, R.Y. Geology, geochemistry and genesis of Xinshan stratiform Diopside rocks in Gejiu, Yunnan. *Acta Mineral. Sin.* **2011**, *31*, 338–352. (In Chinese)

35. Cheng, Y.B.; Mao, J.W.; Yang, Z.X. Geology and vein tin mineralization in the Dadoushan deposit, Gejiu district, SW China. *Miner. Depos.* **2012**, *47*, 701–712. [CrossRef]

36. Nuriel, P.; Weinberger, R.; Kylander–Clark, A.R.C.; Hacker, B.R. Craddock, J.P. The onset of the Dead Sea transform based on calcite age–strain analyses. *Geology* **2017**, *45*, 587–590. [CrossRef]

37. Luo, K.; Zhou, J.X.; Feng, Y.X.; Uysal, T.I.; Nguyen, A.; Zhao, J.X.; Zhang, J.W. In situ U–Pb dating of calcite from the south China antimony metallogenic belt. *iScience* **2020**, *23*, 101–575. [CrossRef]

38. Yang, P.; Wu, G.H.; Nuriel, P.; Nguyen, A.D.; Chen, Y.Q.; Yang, S.; Feng, Y.X.; Ren, Z.L.; Zhao, J.X. In situ LA–ICPMS U–Pb dating and geochemical characterization of fault–zone calcite in the central Tarim Basin, northwest China: Implications for fluid circulation and fault reactivation. *Chem. Geol.* **2021**, *568*, 120–125. [CrossRef]

39. Ludwig, K.R. User's manual for Isoplot/Ex version 3.0: A geochronology toolkit for microsoft excel. *Geochronol. Cent. Spec. Publ.* **2003**, *4*, 1–70.

40. Liu, Y.S.; Hu, Z.C.; Gao, S.; Guünther, D.; Xu, J.; Gao, C.G.; Chen, H.H. In situ analysis of major and trace elements of anhydrous minerals by LA–ICP–MS without applying an internalstandard. *Chem. Geol.* **2008**, *257*, 34–43. [CrossRef]

41. Lin, J.; Liu, Y.S.; Yang, Y.H.; Hu, Z.C. Calibration and correction of LA–ICP–MS and LA–MC–ICP–MS analyses for element contents and isotopic ratios. *Solid Earth Sci.* **2006**, *1*, 5–27. [CrossRef]

42. Paton, C.; Hellstrom, J.; Paul, B.; Woodhead, J.; Hergt, J. Iolite: Freeware for the visualisation and processing of mass spectrometric data. *J. Anal. At. Spectrom.* **2011**, *26*, 2508–2518. [CrossRef]

43. Ubide, T.; Mollo, S.; Zhao, J.X.; Nazzari, M.; Scarlato, P. Sector–zoned clinopyroxene as a recorder of magma history, eruption triggers, and ascent rates. *Geochim. Cosmochim. Acta* **2009**, *251*, 265–283. [CrossRef]

44. Wille, G.; Lerouge, C.; Schmidt, U. A multimodal microcharacterisation of trace–element zonation and crystallographic orientation in natural cassiterite by combining cathodoluminescence, EBSD, EPMA and contribution of confocal Raman–in–SEM imaging. *J. Microsc.* **2018**, *270*, 309–317. [CrossRef]

45. Yang, Z.X.; Mao, J.W.; Chen, M.H.; Tong, X.; Wu, J.D.; Cheng, Y.B.; Zhao, H.J. ^{40}Ar–^{39}Ar dating of muscovite from Laochang veinlet–like Sn deposit in Gejiu tin polymetallic ore district and its geological significance. *Miner. Deposits* **2009**, *28*, 336–344. (In Chinese)

46. Li, Y.S.; Cai, Y.; Chen, J.J.; Chen, N.; Wang, L.; Zhang, Y.K.; He, D.Q. Isotopic dating and geological significance of stratiform orebody in Gejiu tin deposit, Yunnan, China. *Adv. Mater. Res.* **2013**, *616*, 43–47. [CrossRef]

47. Wang, X.J.; Liu, Y.P.; Miao, Y.L.; Bao, T.; Ye, L.; Zhang, Q. In–situ LA–MC–ICP–MS cassiterite U–Pb dating of Dulong Sn–Zn polymetallic deposit and its significance. *Acta Petrol. Sin.* **2014**, *30*, 867–876. (In Chinese)

48. Qin, D.X.; Tan, S.C.; Fan, Z.G.; Li, Y.S.; Chen, A.B.; Li, L.J.; Liu, G.L.; Dang, Y.T.; Tong, X.; Wu, J.D.; et al. Geotectonic evolution and tin–polymetallic metallogenesis in Gejiu–Dachang area. *Acta Mineral. Sin.* **2004**, *24*, 117–123. (In Chinese)

49. Zhou, J.P.; Xu, K.Q.; Hua, R.M.; Zhao, Y.Y. A discussion on genesis of the tin polymetallic sulfide deposits of Southeastern Yunnan. *Yunnan Geol.* **1997**, *16*, 309–349. (In Chinese)

50. Li, Y.S.; Qin, D.X.; Cheng, X.Y.; Guo, N.N.; Luo, X.; Xie, Y.; Zou, T. Evidences of exhalative hydrothermal sedimentary mineralization of Indo–Chinese epoch of Gejiu tin–polymetallic deposits. *Nonferrous Met.* **2009**, *61*, 120–125. (In Chinese)

51. Cheng, Y.B.; Mao, J.W.; Xie, G.Q.; Chen, M.H.; Zhao, C.S.; Yang, Z.X.; Zhao, H.J.; Li, X.Q. Petrogenesis of the Laochang–Kafang granite in the Gejiu area, Yunnan Province: Constraints from geochemistry and zircon U–Pb dating. *Acta Geol. Sin.* **2008**, *82*, 1478–1493. (In Chinese)

52. Cheng, Y.B.; Mao, J.W. Geochronology of the gabbro–mafic microgranular enclaves–granite associations in the Gejiu district, Yunnan province and their geodynamic significance. *Acta Geol. Sin.* **2012**, *86*, 748–761.

53. Zhang, J.; Mao, J.W.; Cheng, Y.B.; Li, X.L. Ar–Ar phlogopite dating of the stratified ore body and muscovite dating of greisens from Xinshan granite intrusion of Kafang tin–copper deoposit in Gejiu area, Yunnan province. *Acta Petrol. Sin.* **2012**, *31*, 1149–1162. (In Chinese)

54. Möller, P.; Dulski, P.; Szacki, W.; Malow, G.; Riedel, E. Substitution of tin in cassiterite by tantalum, niobium, tungsten, iron and manganese. *Geochim. Cosmochim. Acta* **1988**, *52*, 1497–1503. [CrossRef]

55. Hennigh, Q.; Hutchinson, R.W. Cassiterite at Kidd Creek: An example of volcanogenic massive sulfide–hosted tin mineralization. *Econ. Geol. Monogr.* **1999**, *10*, 431–440.

56. Murciego, A.; Sanchez, A.G.; Dusausoy, Y.; Pozas, J.M.M.; Ruck, R. Geochemistry and EPR of cassiterites from the Iberian Hercynian Massif. *Mineral. Mag.* **1997**, *61*, 357–365. [CrossRef]

57. Huang, F.S.; Mu, Z.G.; Chen, C.Y.; Wang, Z.F. The study of isotopic composition of oxygen, hydrogen and carbon in granite of tin deposits, Gejiu. *Acta Petrol. Sin.* **1983**, *2*, 241–247. (In Chinese)

58. Steveson, B.G.; Taylor, R.G. Trace element content of some cassiterites from Eastern Australia. *Proceed. R. Soc. Qld.* **1973**, *84*, 43–54.

59. Schneider, H.J.; Dulski, P.; Luck, J.; Moeller, P.; Villalpando, A. Correlation of trace element distribution in cassiterites and geotectonic position of their deposits in Bolivia. *Miner. Depos.* **1978**, *13*, 119–122. [CrossRef]

60. Moore, F.; Howie, R.A. Geochemistry of some Cornubian cassiterites. *Miner. Depos.* **1979**, *14*, 103–107. [CrossRef]

61. Möller, P.; Dulski, P. Fractionation of Zr and Hf in cassiterite. *Chem. Geol.* **1983**, *40*, 1–12. [CrossRef]

62. Goncharov, G.N.; Filatov, S.K. Typical structural features of cassiterite from Sherlovaya Gora. *Geochem. Int.* **1971**, *8*, 268–275.

63. Izoret, L.; Marnier, G.; Dusausoy, Y. Caractérisation cristallochimique de la cassitérite des gisements d'étain et de tungstène de Galice, Espagne. *Can. Mineral.* **1985**, *23*, 221–231.

64. Heinrich, C.A. The chemistry of tin (–tungsten) ore deposition. *Econ. Geol.* **1990**, *85*, 529–550. [CrossRef]

65. Lehmann, B.; Zoheir, B.A.; Neymark, L.A.; Zeh, A.; Emam, A.; Radwan, A.M.; Zhang, R.Q.; Moscati, R.J. Monazite and cassiterite U–Pb dating of the Abu Dabbab rare–metal granite, Egypt: Late Cryogenian metalliferous granite magmatism in the Arabian–Nubian Shield. *Gondwana Res.* **2020**, *84*, 71–80. [CrossRef]

66. Tindle, A.G.; Breaks, F.W. Oxide minerals of the separation rapids rare–element granitic pegmatite group, northwestern Ontario. *Can. Mineral.* **1998**, *36*, 609–635.

67. Pieczka, A.; Goebiowska, B.; Parafiniuk, J. Geochemistry and origin of the cassiterite from Redziny, Lower Silesia, Poland. *Mineral. Pol.* **2007**, *38*, 219–229. [CrossRef]

68. Shannon, R.D. Revised effective ionic radii and systematic studies of interatomic distances in halides and chalcogenides. *Acta Crystallogr.* **1976**, *A32*, 751–767. [CrossRef]

69. Hoskin, P.W.O.; Schaltegger, U. The composition of zircon and igneous and metamorphic petrogenesis. *Rev. Mineral. Geochem.* **2003**, *53*, 27–62. [CrossRef]

70. Bau, M. Controls on the fractionation of isovalent trace elements in magmatic and aqueous systems: Evidence from Y/Ho, Zr/Hf, and lanthanide tetrad effect. *Contrib. Mineral. Petrol.* **1996**, *123*, 323–333. [CrossRef]

71. Qiu, K.F.; Yu, H.C.; Hetherington, C.; Huang, Y.Q.; Yang, T.; Deng, J. Tourmaline composition and boron isotope signature as a tracer of magmatic-hydrothermal processes. *Am. Mineral.* **2021**, *106*, 1033–1044. [CrossRef]

72. Qiu, K.F.; Yu, H.C.; Wu, M.Q.; Geng, J.Z.; Ge, X.K.; Gou, Z.Y.; Taylor, R.D. Discrete Zr and REE mineralization of the Baerzhe rare–metal deposit, China. *Am. Mineral.* **2019**, *104*, 1487–1502. [CrossRef]

73. Qiu, K.F.; Yu, H.C.; Deng, J.; McIntire, D.; Gou, Z.Y.; Geng, J.Z.; Chang, Z.S.; Zhu, R.; Li, K.N.; Goldfarb, R.J. The giant Zaozigou orogenic Au-Sb deposit in West Qinling, China: Magmatic or metamorphic origin? *Miner. Depos.* **2020**, *55*, 345–362. [CrossRef]